INI and ICI in Mixed-Numerology MIMO-OFDM Systems in Spatially Correlated Time-Varying Wideband Channels: Analysis and Mitigation

Tenneti Venkata Satya Sreedhar and Neelesh B. Mehta, *Fellow, IEEE*

***Abstract*—5G new radio (NR) is based on the mixed-numerology multiple-input multiple-out (MIMO) orthogonal frequency division multiplexing (OFDM) physical layer. Unlike conventional single-numerology systems, subcarriers of different numerologies interfere with each other. The larger Doppler spreads and phase noise that occur at higher speeds and carrier frequencies make the channel vary with time, which affects inter-numerology interference (INI) and exacerbates inter-carrier interference (ICI). We derive novel insightful expressions for the INI and ICI covariances for a mixed-numerology, multi-user MIMO-OFDM system in a wideband spatially correlated time-varying channel with phase noise. On the other hand, the literature has only studied simpler single-input single-out systems or MIMO channels with several limitations. With this analytical foundation, we propose a first-of-its-kind joint INI and ICI mitigation technique that is based on statistical information and incorporates fairness. We derive the precoder for each user that achieves the single-user ergodic capacity. We also determine a novel power allocation that maximizes the weighted sum rate. We solve this using an iterative algorithm based on the difference of convex programming framework. The proposed approach achieves a higher weighted sum rate than several benchmarks. Our results highlight the joint impact of INI and ICI and the influence of various system parameters.**

***Index Terms*—Mixed-numerology, Inter-numerology interference, Inter-carrier interference, OFDM, MIMO, Antenna correlation, Doppler spread.**

I. Introduction

The fifth generation (5G) new radio (NR) standard is designed to meet the requirements of diverse use cases, which include enhanced mobile broadband (eMBB), massive machine-type communications (mMTC), and ultra-reliable and low-latency communications (URLLC). eMBB provides high data rates up to 20 Gbps, URLLC supports latencies smaller than 1 millisecond and extremely high reliability, and mMTC supports a high connection density up to 1 million devices/km^2 [2]. Even more aggressive targets are envisaged in 6G [3].

To satisfy the diverse requirements of the services, mixed-numerology orthogonal frequency division multiplexing (OFDM) has been introduced in 5G systems. This is a first step towards the flexible physical layer envisaged for 6G. A numerology specifies the parameters of an OFDM waveform such as subcarrier spacing and cyclic prefix (CP) length. Subcarrier spacings of 15, 30, and 60 kHz are used in the sub-6 GHz band. On the other hand, in the millimeter wave bands, larger subcarrier spacings up to 960 kHz are used to alleviate the effect of phase noise and limit the discrete Fourier transform (DFT) size. However, mixed-numerology OFDM systems suffer from inter-numerology interference (INI) between subcarriers belonging to distinct numerologies even though these subcarriers occupy non-overlapping time-frequency blocks.

Several works in the literature analyze the INI for single-input single-output (SISO)-OFDM systems and propose techniques to mitigate it [4]–[9]. However, the analysis and mitigation of INI in multiple-input-multiple-output (MIMO)-OFDM systems over time-varying fading channels has received much less attention. This is an important problem because MIMO, in combination with OFDM, is a key technology that underpins the 5G physical layer and enables it to achieve high spectral efficiency and reliability. The analysis of MIMO systems is more sophisticated than for SISO systems due to the richer and larger space of MIMO channels. Furthermore, practical deployments necessarily have to work in time-varying channels.

Broadly, two classes of MIMO precoder designs have been studied in the literature. In statistical channel state information (CSI)-based precoders, the precoding is adapted based on channel statistics, such as transmit and receive spatial correlation [10]. Whereas, in instantaneous CSI-based precoders, the precoding is adapted based on the instantaneous channel condition. The latter requires feedback at least once in a coherence interval from the receiver to the transmitter, which then adapts its precoder and rate. When the channel varies faster, the feedback overhead increases. Such frequent feedback is not needed in statistical CSI-based precoders.

The time-variations in the channel also cause a loss of orthogonality among the subcarriers of the same numerology. This generates inter-carrier interference (ICI) and affects the INI [11]. Instabilities in the local oscillators used for generating the carriers at the transmitter and the receiver, which cause phase noise, aggravate these time variations [12], [13]. The effects of phase noise are more severe at higher carrier frequencies [14]. A comprehensive analysis of INI in MIMO-OFDM systems with time-varying fading channels and phase noise is, therefore, necessary to efficiently operate 5G and beyond systems.

T. V. S. Sreedhar is with the Central Research Laboratory at Bharat Electronics Limited, Bengaluru, India (Email: sreedhartenneti@gmail.com). N. B. Mehta is with the Dept. of Electrical Communication Eng. at the Indian Institute of Science (IISc), Bengaluru, India (Email: nbmehta@iisc.ac.in).

Some results related to this manuscript have been presented in the National Conf. Commun. (NCC), Mar. 2025 [1].

A. Literature Survey

We first summarize the literature on INI in SISO-OFDM and MIMO-OFDM systems and then on ICI, and point out some shortcomings.

a) INI in SISO-OFDM Systems: Expressions for the INI power as a function of the frequency offset between the interfering and victim subcarriers are derived in [4]. However, a time-invariant channel is assumed. Expressions for the fading-averaged INI power in the presence of phase noise for time-varying channels are derived in [9]. A subcarrier power allocation method is proposed in [15] to maximize the packet arrival rate that can be supported by the mixed-numerology system subject to a packet delay requirement. A spectrally efficient way of implementing the guard band to reduce the INI is proposed in [16]. In [6], an instantaneous-CSI based joint subcarrier and power allocation scheme is proposed to deal with the INI in a coordinated multi-point system. However, all the above works focus on SISO. Also, they do not consider phase noise, with the exception of [9].

b) INI in MIMO-OFDM Systems: In [5], an instantaneous-CSI based zero-forcing (ZF) precoding is proposed to nullify the INI in massive MIMO downlink systems, but only when the number of transmit antennas is greater than or equal to the number of subcarriers. Linear detectors are proposed to mitigate the INI in [17] for massive MIMO uplink systems. An INI cancellation scheme is proposed for deterministic channels in [18] for a massive-MIMO OFDM uplink receiver. A suppression scheme at the transmitter to mitigate the INI in a massive-MIMO OFDM downlink is proposed in [19]. However, none of these works consider time-varying fading channels, spatial correlation, phase noise, or fairness. Another major shortcoming of these works is that they focus on only single-antenna users. Table I summarizes the relevant literature on INI.

c) ICI in MIMO-OFDM Systems: Given the vast literature on ICI, which also arises in conventional single-numerology OFDM systems, we limit our discussion to MIMO-OFDM systems. We refer the reader to [20] for the literature on ICI in SISO systems. The ICI covariance is derived for fading channels in [11]. Time-domain filtering methods at the receiver to mitigate ICI are also proposed. To mitigate ICI, ZF equalization is proposed in [21] and frequency-domain partial response coding is proposed in [22]. However, spatial correlation is not considered in [11], [21], [22]. In [23], the precoder and power allocation are numerically determined for time-varying channels. However, perfect instantaneous CSI is assumed at the transmitter. Furthermore, the time variation of the channel within an OFDM symbol is assumed to follow a linear curve. A robust precoder design is proposed in [24] for the Kronecker channel correlation model, but it only applies to the massive MIMO regime.

B. Focus and Contributions

We derive novel expressions for the INI and ICI covariance matrices in the downlink of a mixed-numerology MIMO-OFDM system. Our model is more comprehensive and novel compared to the literature as it accounts for spatial correlation, time variations due to Doppler spread, phase noise, guard bands, and partially occupied subcarriers. It applies to the entire family of numerologies in 5G NR. Lastly, we propose a first-of-its-kind transmit-signal covariance design that jointly mitigates INI and ICI. We make the following contributions:

- For a spatially correlated, wideband MIMO fading channel that varies in time due to both Doppler and phase noise, we derive novel, insightful closed-form expressions for the INI and ICI covariance matrices. Spatial correlation arises only in MIMO channels and not in SISO channels. It depends on the antenna spacing and scattering in the environment. We study the Kronecker spatial correlation model, which is widely used for link-level simulations and on which the tapped delay line (TDL) and clustered delay line (CDL) models defined in the 3GPP standards are based [25].
  We show that the INI and ICI covariances are proportional to the receive spatial correlation matrix, while the proportionality constants depend on the transmit spatial correlation. In addition, the constants also depend on the temporal auto-correlation of the channel, phase noise auto-correlation, and transmit signal covariances of the users. Such an analysis is essential for a system designer to quantitatively understand the dependence of INI and ICI on key system parameters such as Doppler spread, phase noise bandwidth, and spatial correlation.
- With the above analytical foundation, we then develop a novel transmit-side precoding and power allocation technique that jointly mitigates INI and ICI. Here, we make the following two contributions:
  1) We show that the optimal precoder that achieves the single-user ergodic capacity in the presence of both ICI and INI is the matrix of eigenvectors of the transmit spatial correlation matrix. The combined influence of INI, ICI, phase noise, and spatial correlation on the precoder design has not been studied in the literature.
  2) For the above precoder, we present a novel problem formulation that optimizes the allocation of powers to the spatial eigenmodes of the MIMO channels of the users to maximize the weighted sum rate. We employ an iterative algorithm based on successive convex approximation (SCA) to solve the problem. The algorithm provably converges to an allocation that locally maximizes the weighted sum rate. While SCA is well known, the novelty of our approach lies in its accounting for the combined effect of INI and ICI, which make the optimization problem non-convex and different from the statistical CSI-based power allocation considered in the literature. Our approach also incorporates user fairness, which has received limited attention in the literature on INI in both SISO-OFDM and MIMO-OFDM systems.
- Our approach achieves a larger weighted sum rate than several benchmarks that are based on existing works and also variations that help understand the effect of the precoder or the power allocation. We find that ICI and INI can lead to solutions that are non-intuitive at

first sight where less power is assigned to the stronger MIMO eigenmodes compared to the weaker ones at larger Doppler spreads or phase noise bandwidths. Our numerical results bring out how the numerology affects the power allocation.

Comparisons: Our results differ from those in [5], [17]–[19], which study only a given or deterministic channel realization. However, in practice, channel models are specified in terms of a power delay profile, which generates an ensemble of channel realizations. These works also do not consider phase noise or time variations. Another difference is that our precoder and power allocation are based on statistical CSI. On the other hand, the approaches in [5], [19], [23] require instantaneous CSI, which entails a larger feedback overhead. Unlike the method in [24], our work is applicable in all antenna regimes.

The results in [11], which focuses only on ICI and assumes a spatially white MIMO channel, are a special case of our work. Our manuscript also generalizes the result in [10] to a MIMO-OFDM system with INI, ICI, and phase noise.

C. Outline and Notation

Section II presents the mixed-numerology MIMO-OFDM system model. In Section III, we analyze INI and ICI. In Section IV, we derive the optimal transmit precoders and power allocation matrices. Numerical results are presented in Section V. Our conclusions follow in Section VI.

Notation: The notation $X \sim \mathcal{CN}(\sigma^2)$ means that X is a zero-mean, circularly symmetric complex Gaussian random variable (RV) with variance σ^2. And, $X \sim Y$ means that X and Y have the same probability distribution. We use lower-case bold letters for vectors and upper-case bold letters for matrices. The expectation with respect to an RV X is denoted by $\mathbb{E}_X[\cdot]$; the subscript is dropped when X is obvious from the context. We denote the conjugate by $(\cdot)^*$, transpose by $(\cdot)^T$, and Hermitian transpose by $(\cdot)^\dagger$. The inner product $\mathrm{Tr}\left\{\mathbf{B}^\dagger\mathbf{A}\right\}$ between two matrices $\mathbf{A}$ and $\mathbf{B}$ is denoted by $\langle\mathbf{A},\mathbf{B}\rangle$. We denote the covariance of a random vector $\mathbf{x}$ by $\mathrm{Cov}\,(\mathbf{x})$. For a matrix $\mathbf{A}$, we denote its i^{th} row by $\mathbf{A}_{i*}$, j^{th} column by $\mathbf{A}_{*j}$, and $(i,j)^{\text{th}}$ element by $\mathbf{A}_{i,j}$ or $[\mathbf{A}]_{i,j}$. The $n \times n$ identity matrix is denoted by $\mathbf{I}_n$. The notation $\mathbf{A} \succeq \mathbf{0}$ means that $\mathbf{A}$ is a positive semi-definite matrix. We denote the gradient with respect to $\mathbf{A}$ by $\nabla_{\mathbf{A}}$. We denote the sequence $X_0, X_1, \ldots, X_{K-1}$ by $\{X_k\}_{k=0}^{K-1}$, and the sequence of matrices $\left\{\mathbf{A}^{(i)}\right\}_{i=1,i\neq k}^{K}$ by $\mathbf{A}^{(\setminus k)}$.

II. System Model

We consider a mixed-numerology MIMO-OFDM downlink system with K users. The base station (BS) has M_t transmit antennas and each user has M_r receive antennas.

We first define a base numerology 0. It has a subcarrier spacing $b^{(0)} = 15$ kHz and CP of duration $\mathrm{CP}_0 = 4.7$ μs. For a numerology ℓ, the DFT length is N_ℓ, the subcarrier bandwidth is $b^{(\ell)}$, and the CP length is CP_ℓ. In 5G NR, $b^{(\ell)}$ and CP_ℓ are related to the base numerology as follows:

$$b^{(\ell)} = 2^\ell b^{(0)} \text{ and } \mathrm{CP}_\ell = \frac{\mathrm{CP}_0}{2^{\mu_\ell}}, \tag{1}$$

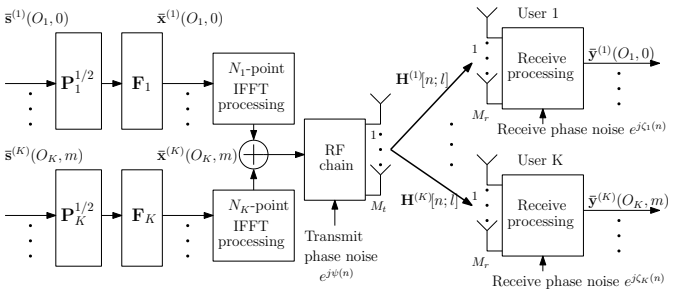

Fig. 1. System model for a mixed-numerology downlink MIMO-OFDM system with K users.

where $\ell \in \{0,1,2,\ldots,6\}$. The numerology that can be assigned depends on the frequency band of operation. The bands are divided into three frequency ranges (FR), namely FR1, FR2-1, and FR2-2 [33, Chap. 28]. For data transmission, $\ell \in \{0,1,2\}$ in FR1, $\ell \in \{2,3\}$ in FR2-1, and $\ell \in \{3,5,6\}$ in FR2-2. Note that $\ell = 4$ is not used for data transmission.

In 5G NR, each user can be assigned multiple bandwidth parts. A bandwidth part is a set of contiguous physical resource blocks over which the BS can transmit data to the user. Only one among the assigned bandwidth parts can be active at any time. The user only needs to look in the active bandwidth part for its signal. Let user k be assigned an active bandwidth part with numerology ℓ_k. Let the number of contiguous subcarriers allocated to it be Z_ℓ. Notice that FR1, FR2-1, and FR2-2 each support at most three numerologies. Therefore, when $K \geq 4$, some of the users will have the same numerology.

The transmitted vector signal $\mathbf{x}[n] \in \mathbb{C}^{M_t \times 1}$ in baseband at time sample n in this system is given by

$$\mathbf{x}[n] = e^{j\psi[n]} \sum_{k=1}^{K} \mathbf{x}^{(k)}[n], \tag{2}$$

where the vector $\mathbf{x}^{(k)}[n] \in \mathbb{C}^{M_t \times 1}$ is the signal of user k and $\psi[n]$ is the phase noise due to the transmitter.

For user k, $\mathbf{x}^{(k)}[n]$ is given by

$$\mathbf{x}^{(k)}[n] = \frac{1}{\sqrt{Z_k M_t}} \sum_{u=O_k}^{O_k+Z_k-1} \sum_{v=-\infty}^{\infty} \bar{\mathbf{x}}^{(k)}[u,v] g^{(k)}[n - vN_k^T] \times e^{j\frac{2\pi}{N_k} u\left(n - \mathrm{CP}_k - vN_k^T\right)}, \tag{3}$$

where $\bar{\mathbf{x}}^{(k)}[u,v] \in \mathbb{C}^{M_t \times 1}$ is the precoded symbol vector of subcarrier u of OFDM symbol v, N_k^T is the number of samples in the OFDM symbol duration including the CP, O_k is the numerology's offset, and $N_k^T = N_k + \mathrm{CP}_k$. This general formulation allows for arbitrary-sized guard bands between the users. The OFDM symbol duration $T_s^{(k)}$ equals $N_k T_{\text{samp}}$, where T_{samp} is the sampling duration. The transmit window $g^{(k)}[n]$ is 1, for $0 \leq n < N_k^T$, and is 0, otherwise.

The precoded symbol vector $\bar{\mathbf{x}}^{(k)}[u,v]$ can be written in terms of the information symbol vector $\mathbf{s}^{(k)}[u,v]$ and the unitary precoder $\mathbf{F}_k$ as

$$\bar{\mathbf{x}}^{(k)}[u,v] = \mathbf{F}_k \left(\mathbf{P}^{(k)}\right)^{1/2} \mathbf{s}^{(k)}[u,v], \tag{4}$$

TABLE I
LITERATURE ON INI IN MIXED-NUMEROLOGY OFDM SYSTEMS

Reference	*Channel model*	*Doppler spread*	*Phase noise*	*SISO/MIMO*	*Fairness*	*Mitigation technique*
Zhang et al. [4]	Deterministic	No	No	SISO	No	Cancellation at receiver
Chen et al. [26]	Deterministic	No	No	SISO	No	–
Mao et al. [27]	Deterministic	No	No	SISO	Yes	Power allocation
Shen et al. [6]	Deterministic	No	No	SISO	Yes	Subcarrier and power allocation
Su et al. [15]	Block fading	No	No	MISO	No	Power allocation across subcarriers
Memisoglu et al. [16]	Block fading	No	No	SISO	No	Method for implementing guard bands
Kihero et al. [28]	AWGN	No	No	SISO	No	Common CP insertion
Marijanovic et al. [29]	AWGN	No	No	SISO	No	–
Mao et al. [30]	AWGN (continuous-time)	No	No	SISO	No	–
Choi et al. [31]	Block fading (flat)	No	No	SISO	No	Spreading and combining at transmitter cancellation at receiver
Zhang et al. [32]	Deterministic	No	Yes	SISO	No	Cancellation at receiver
Sreedhar et al. [9]	Time-varying	Yes	Yes	SISO	No	Power allocation across subcarriers
Son et al. [5]	Deterministic	No	No	MIMO	No	ZF precoding at transmitter
Son et al. [17]	Deterministic	No	No	MIMO	No	Linear combining at receiver
Cheng et al. [19]	Deterministic	No	No	MIMO	No	Pre-cancellation at transmitter
Cheng et al. [18]	Deterministic	No	No	MIMO	No	Cancellation at receiver
Proposed work	Time-varying	Yes	Yes	MIMO	Yes	Precoder and power allocation across eigenmodes

where $\mathbf{P}^{(k)}$ is a diagonal power allocation matrix. The components of $\mathbf{s}^{(k)}[u,v]$ are zero-mean and uncorrelated. Thus, $\mathbb{E}\left[\mathbf{s}^{(k)}[u,v]\mathbf{s}^{(k)\dagger}[u,v]\right]=\mathbf{I}_{M_t}$.

From above, the transmit power of user k is $Z_k\mathrm{Tr}\left\{\mathbf{P}^{(k)}\right\}$. In 5G, the powers are operationally specified in terms of the energy-per-resource-element (EPRE) EP_k, which is defined as $\mathsf{EP}_k = N_k\mathrm{Tr}\left\{\mathbf{P}^{(k)}\right\}/M_t$ for user k. A key point to note is that the ratio of EPREs of two users can exhibit a large dynamic range from -32 dB to 32 dB [34, Ch. 13].

After passing through a wideband, frequency-selective channel, the n^{th} time-sample of the received signal $\mathbf{y}^{(k)}[n]\in\mathbb{C}^{M_r\times 1}$ for the user with numerology k is given by

$$\mathbf{y}^{(k)}[n]=\sqrt{\beta_k}e^{j\phi_k[n]}\sum_{\tau=0}^{L-1}\mathbf{H}^{(k)}[n;\tau]\,\mathbf{x}[n-\tau]+\mathbf{z}^{(k)}(n), \quad (5)$$

where $\left\{\mathbf{H}^{(k)}[n;\tau]\right\}_{\tau=0}^{L-1}$ are the time-domain channel tap matrices of user k, which represent small-scale fading, β_k is the pathloss for user k, $\phi_k[n]$ is the sum of the phase noise $\psi[n]$ at the BS and the phase noise $\zeta_k[n]$ at user k's receiver, and $\mathbf{z}^{(k)}(n)$ is additive white Gaussian noise (AWGN) at user k's receiver. Here, τ tracks the tap-delays. The effective phase noise $\phi_k[n]$ is a Wiener process with two-sided 3-dB bandwidth Ω_k. Its auto-correlation is given by [35], [36]

$$\mathbb{E}\left[e^{j\phi_k[n_1]}e^{-j\phi_k[n_2]}\right]=e^{-\pi|n_1-n_2|\Omega_k T_{\text{samp}}}. \quad (6)$$

MIMO Channel Model: The $(i,j)^{\text{th}}$ entry of $\mathbf{H}^{(k)}[n;\tau]$ is denoted by $h_{i,j}^{(k)}[n;\tau]$. As per the wide-sense stationary and uncorrelated scattering model (WSSUS) [37, Ch. 3], $\left\{h_{i,j}^{(k)}[n;\tau]\right\}_{\tau=0}^{L-1}$ are zero-mean, wide-sense stationary, and uncorrelated for all (n,τ). The WSSUS assumption underpins all the channel profiles, such as TDL and CDL, specified by 3GPP.

The transmit and receive spatial correlation matrices for user k are given by $\mathbf{T}^{(k)}$ and $\mathbf{R}^{(k)}$, respectively [38]. Here, $\mathbf{T}_{j,j'}^{(k)} = \mathbb{E}\left[h_{i,j}^{(k)*}[n;\tau]\,h_{i,j'}^{(k)}[n;\tau]\right]$, $\forall n,\tau,i$, and $\mathbf{R}_{i,i'}^{(k)} = \mathbb{E}\left[h_{i,j}^{(k)}[n;\tau]\,h_{i',j}^{(k)*}[n;\tau]\right]$, $\forall n,\tau,j$. Let the eigenvalue decompositions of $\mathbf{T}^{(k)}$ and $\mathbf{R}^{(k)}$ be $\mathbf{T}^{(k)}=\mathbf{U}_T^{(k)}\mathbf{\Delta}_T^{(k)}\mathbf{U}_T^{(k)\dagger}$ and $\mathbf{R}^{(k)}=\mathbf{U}_R^{(k)}\mathbf{\Delta}_R^{(k)}\mathbf{U}_R^{(k)\dagger}$, where $\mathbf{U}_T^{(k)}\in\mathbb{C}^{M_t\times M_t}$ and $\mathbf{U}_R^{(k)}\in\mathbb{C}^{M_r\times M_r}$ are unitary matrices.

In terms of the power angular spectrum (PAS) $S_r^{(k)}$, the receive spatial correlation $\mathbf{R}_{i,j}^{(k)}$ between antennas i and j of user k is given by [39, Ch. 3]

$$\mathbf{R}_{i,j}^{(k)}=\int_{-\pi}^{\pi}S_r^{(k)}(\theta)\,e^{j2\pi|i-j|d_r\cos(\theta)}\,d\theta, \quad (7)$$

where d_r is the wavelength-normalized inter-antenna spacing. For example, for the Laplacian PAS adopted by 3GPP [25],

$$S_r^{(k)}(\theta)=\frac{1}{\sqrt{2}s_r^{(k)}}e^{-\frac{\sqrt{2}\left|\theta-m_r^{(k)}\right|}{s_r^{(k)}}}, \quad (8)$$

where $m_r^{(k)}$ and $s_r^{(k)}$ are the mean and standard deviation, respectively, of the angles-of-arrival at user k. The transmit spatial correlation $\mathbf{T}_{i,j}^{(k)}$ between antennas i and j of the BS is given by a similar formula in terms of the mean $m_t^{(k)}$ and standard deviation $s_t^{(k)}$ of the angles-of-departure from the BS to user k.

Time Variations Model: The temporal auto-correlation $r_\tau^{(k)}[w]$ of $h_{i,j}^{(k)}[n;\tau]$ is defined as

$$r_\tau^{(k)}[w]\triangleq\mathbb{E}\left[h_{i,j}^{(k)}[n+w;\tau]\,h_{i,j}^{(k)*}[n;\tau]\right]=r_\tau^{(k)}[0]\tilde{r}^{(k)}[w]. \quad (9)$$

Here, $r_\tau^{(k)}[0]$ accounts for the dependency on the tap-delay index τ. When viewed as a function of τ, $r_\tau^{(k)}[0]$ gives the power delay profile (PDP). Thus, $\tilde{r}^{(k)}[w]$ is a normalized temporal auto-correlation function. Without loss of generality, let $\sum_{\tau=0}^{L-1}r_\tau^{(k)}[0]=1$. The temporal auto-correlation $r_\tau^{(k)}[w]$ depends on the Doppler spread $f_d^{(k)}$ of user k.

The WSSUS model implies that the statistics of the MIMO channels of the different subcarriers are the same [40]. Note, however, that the MIMO channel realizations of different

subcarriers are different with probability 1. Hence, we use the same precoder and power allocation for all the subcarriers of a user. From (4), the transmit signal covariance $\mathbf{Q}^{(k)}$ equals

$$\mathbf{Q}^{(k)} = \mathbb{E}\left[\bar{\mathbf{x}}^{(k)}[u,v]\bar{\mathbf{x}}^{(k)\dagger}[u,v]\right] = \mathbf{F}_k\mathbf{P}^{(k)}\mathbf{F}_k^{\dagger}. \quad (10)$$

III. INI and ICI Analysis

Substituting (2) in (5), the expression for $\mathbf{y}^{(k)}[n]$ becomes

$$\mathbf{y}^{(k)}[n] = \sqrt{\beta_k}e^{j\phi_k[n]}\sum_{\tau=0}^{L-1}\mathbf{H}^{(k)}[n;\tau]\sum_{l=1}^{K}\mathbf{x}^{(l)}[n-\tau] + \mathbf{z}^{(k)}(n). \quad (11)$$

Note that at user k's receiver, the signals of all users pass through the same channel $\mathbf{H}^{(k)}[n;\tau]$ and are perturbed by the same phase-noise and AWGN. The receiver performs an N_k-point DFT after removing the CP of length $\text{CP}_k \geq L-1$. The demodulated signal $\bar{\mathbf{y}}^{(k)}[p,m]$ at subcarrier p of OFDM symbol m is given by

$$\bar{\mathbf{y}}^{(k)}[p,m] = \frac{1}{\sqrt{N_k}}\sum_{n=-\infty}^{\infty}\mathbf{y}^{(k)}[n]\,q^{(k)}[n-mN_k^T] \times e^{-j\frac{2\pi}{N_k}p\left[n-\text{CP}_k-mN_k^T\right]}, \quad (12)$$

where $q^{(k)}[n]$ is the rectangular receive window. It is 1 for $\text{CP}_k \leq n < N_k^T$, and is 0 otherwise.

From (3), (11), and (12), we notice that $\bar{\mathbf{y}}^{(k)}[p,m]$ is the summation of the precoded information symbol vectors of the users. Since the symbols of different users are mutually independent, the covariance $\overline{\mathbf{K}}_{\text{INI}}^{(k)}(p)$ of the total INI at subcarrier p of user k due to all other users is given by

$$\overline{\mathbf{K}}_{\text{INI}}^{(k)}(p) = \sum_{l=1,l\neq k}^{K}\mathbf{K}_{\text{INI}}^{(k)}(p,\mathbf{Q}^{(l)}), \quad (13)$$

where $\mathbf{K}_{\text{INI}}^{(k)}(p,\mathbf{Q}^{(l)})$ is the covariance of the INI at subcarrier p of user k due to user l alone. It follows that it is sufficient to first derive the INI covariances for any two users, say a and b. Substituting these covariances in the summation in (13) for each user pair (k,l), while giving due consideration to the ratio of subcarrier spacings of the users k and l, gives the total INI covariance for a user. When there are more users than numerologies, some of the users will have the same numerology. These users do not cause INI to each other. Thus, $\mathbf{K}_{\text{INI}}^{(k)}(p,\mathbf{Q}^{(l)}) = \mathbf{0}$ when users k and l have the same numerology.

We now analyze the INI between any two users a and b with different numerologies. Without loss of generality, let user a have a narrower subcarrier spacing than user b. Let

$$\mu = \log_2\left(b^{(\ell_b)}/b^{(\ell_a)}\right). \quad (14)$$

Thus, the OFDM symbol duration of user a is 2^μ times that of user b.

We introduce the following notation:

- The interference due to $\bar{\mathbf{x}}^{(b)}[q,v]$, which is transmitted on subcarrier q and OFDM symbol v of user b, seen at subcarrier p and OFDM symbol m of user a is $\mathbf{G}^{(a,b)}(p,m,q,v)\bar{\mathbf{x}}^{(b)}[q,v]$. As we shall see below, the $(i,j)^{\text{th}}$ element of $\mathbf{G}^{(a,b)}(p,m,q,v)$ is given by

$$\mathbf{G}_{i,j}^{(a,b)}(p,m,q,v) = \sqrt{\beta_a}\sum_{n=-\infty}^{\infty}e^{j\phi_a[n]}\sum_{\tau=0}^{L-1}h_{i,j}^{(a)}[n;\tau] \times \frac{1}{\sqrt{N_b}}g^{(b)}[n-vN_b^T-\tau]e^{j\frac{2\pi}{N_b}q\left[n-\text{CP}_b-vN_b^T-\tau\right]} \times\left(\frac{1}{\sqrt{N_a}}q^{(a)}[n-mN_a^T]e^{j\frac{2\pi}{N_a}p\left[n-\text{CP}_a-mN_a^T\right]}\right)^*. \quad (15)$$

  The notation is involved, but required, as we need to track the transmit and receive antennas, subcarrier, and symbol indices of all users.
- The instantaneous INI and ICI at subcarrier p and OFDM symbol m of user a are denoted by $\mathsf{INI}_a[p,m] \in \mathbb{C}^{M_r\times 1}$ and $\mathsf{ICI}_a[p,m] \in \mathbb{C}^{M_r\times 1}$, respectively.

2^μ OFDM symbols of user b overlap in time-domain with an OFDM symbol of user a. Thus, without loss of generality, let us consider symbol 0 of user a and symbols $\{0,1,\ldots,2^\mu-1\}$ of user b. From (12), the frequency-domain signal $\bar{\mathbf{y}}^{(a)}[p,0]$ received by user a at subcarrier p and OFDM symbol 0 can be decomposed as follows:

$$\bar{\mathbf{y}}^{(a)}[p,0] = \mathbf{G}^{(a,a)}(p,0,p,0)\bar{\mathbf{x}}^{(a)}[p,0] + \mathsf{ICI}_a[p,0] + \mathsf{INI}_a[p,0] + \bar{\mathbf{z}}^{(a)}[p,0]. \quad (16)$$

Here, $\mathsf{ICI}_a[p,0]$ is the sum of the interferences due to all the subcarriers of user a (excluding subcarrier p), $\mathsf{INI}_a[p,0]$ is the sum of the interferences due to all the subcarriers of user b, and $\bar{\mathbf{z}}^{(a)}[p,0]$ is the noise on subcarrier p. After some algebra, the interferences $\mathsf{ICI}_a[p,0]$ and $\mathsf{INI}_a[p,0]$ can be shown to be

$$\mathsf{ICI}_a[p,0] = \sum_{q=O_a,q\neq p}^{O_a+Z_a-1}\mathbf{G}^{(a,a)}(p,0,q,0)\bar{\mathbf{x}}^{(a)}[q,0], \quad (17)$$

$$\mathsf{INI}_a[p,0] = \sum_{v=0}^{2^\mu-1}\sum_{q=O_b}^{O_b+Z_b-1}\mathbf{G}^{(a,b)}(p,0,q,v)\bar{\mathbf{x}}^{(b)}[q,v]. \quad (18)$$

Similarly, the frequency-domain signal received by user b at subcarrier p and OFDM symbol $m \in \{0,1,\ldots,2^\mu-1\}$ is

$$\bar{\mathbf{y}}^{(b)}[p,m] = \mathbf{G}^{(b,b)}(p,m,p,m)\bar{\mathbf{x}}^{(b)}[p,m] + \mathsf{ICI}_b[p,m] + \mathsf{INI}_b[p,m] + \bar{\mathbf{z}}^{(b)}[p,m]. \quad (19)$$

Here, $\mathsf{ICI}_b[p,m]$ is the sum of the interferences due to all the subcarriers of user b (excluding subcarrier p), $\mathsf{INI}_b[p,m]$ is the sum of the interferences due to all the subcarriers of user a, and $\bar{\mathbf{z}}^{(b)}[p,m]$ is the noise at subcarrier p. Here,

$$\mathsf{ICI}_b[p,m] = \sum_{q=O_b,q\neq p}^{O_b+Z_b-1}\mathbf{G}^{(b,b)}(p,m,q,m)\bar{\mathbf{x}}^{(b)}[q,m], \quad (20)$$

$$\mathsf{INI}_b[p,m] = \sum_{q=O_a}^{O_a+Z_a-1}\mathbf{G}^{(b,a)}(p,m,q,0)\bar{\mathbf{x}}^{(a)}[q,0]. \quad (21)$$

Comment: The ICI at a user is due to its own information symbols. Therefore, the summation in (17) is over the subcarriers (except subcarrier p) occupied by user a in OFDM symbol 0. Similarly, the summation in (20) is over the subcarriers (except subcarrier p) occupied by user b in

OFDM symbol m. On the other hand, INI is caused by the overlapping OFDM symbols of the interfering user. Hence, (18) has a double summation; the inner summation is over all the subcarriers occupied by user b and the outer summation is over its 2^μ symbols. On the other hand, in (21), there is only one summation that accounts for the subcarriers occupied in OFDM symbol 0 by user a.

A. INI Analysis

We now derive closed-form expressions for $\mathbf{K}_{\text{INI}}^{(a)}(p, \mathbf{Q}^{(b)})$ and $\mathbf{K}_{\text{INI}}^{(b)}(p, \mathbf{Q}^{(a)})$.

Result *1:* The covariance matrix $\mathbf{K}_{\text{INI}}^{(a)}(p, \mathbf{Q}^{(b)})$ of the INI at subcarrier p of user a is given by

$$\mathbf{K}_{\text{INI}}^{(a)}(p, \mathbf{Q}^{(b)}) = \gamma_{\text{INI}}^{(a,b)}(p) \left\langle \mathbf{Q}^{(b)}, \mathbf{T}^{(a)} \right\rangle \mathbf{R}^{(a)}, \tag{22}$$

where

$$\gamma_{\text{INI}}^{(a,b)}(p) = \frac{\beta_a}{N_a Z_b M_t} \sum_{q=O_b}^{O_b+Z_b-1} \sum_{\tau=0}^{L-1} \Bigg[\sum_{w=-(M+\tau-1)}^{M+\tau-1} (M+\tau-|w|) \times r_\tau^{(a)}[w] e^{-\pi|w|\Omega_a T_{\text{samp}}} e^{j\frac{2\pi}{N_a}(2^\mu q-p)w} + (2^\mu - 2) \times \sum_{w=-(N_b^T-1)}^{N_b^T-1} (N_b^T - |w|) r_\tau^{(a)}[w] e^{-\pi|w|\Omega_a T_{\text{samp}}} e^{j\frac{2\pi}{N_a}(2^\mu q-p)w} + \sum_{w=-(N_b^T-\tau-1)}^{N_b^T-\tau-1} (N_b^T-\tau-|w|) r_\tau^{(a)}[w] e^{-\pi|w|\Omega_a T_{\text{samp}}} e^{j\frac{2\pi}{N_a}(2^\mu q-p)w} \Bigg], \tag{23}$$

and $M = N_b^T - \text{CP}_a$.

Proof: The proof is given in Appendix A. ∎

Result 1 shows that $\mathbf{K}_{\text{INI}}^{(a)}(p, \mathbf{Q}^{(b)}) \propto \mathbf{R}^{(a)}$. The scaling constant $\gamma_{\text{INI}}^{(a,b)}(p)$ captures the combined effect of the temporal auto-correlation of user a's channel, which depends on the user a's Doppler spread and the subcarriers allocated to user b. It is also an exponential function of the 3-dB bandwidth Ω_a of the effective phase noise at user a. The covariance is also proportional to the inner-product of the transmit spatial correlation matrix $\mathbf{T}^{(a)}$ of user a's channel and the transmit signal covariance $\mathbf{Q}^{(b)}$ of user b.

Result *2:* The covariance matrix $\mathbf{K}_{\text{INI}}^{(b)}(p, \mathbf{Q}^{(a)})$ of the INI at subcarrier p of user b is given by

$$\mathbf{K}_{\text{INI}}^{(b)}(p, \mathbf{Q}^{(a)}) = \gamma_{\text{INI}}^{(b,a)}(p) \left\langle \mathbf{Q}^{(a)}, \mathbf{T}^{(b)} \right\rangle \mathbf{R}^{(b)}, \tag{24}$$

where

$$\gamma_{\text{INI}}^{(b,a)}(p) \triangleq \frac{\beta_b}{N_b Z_a M_t} \sum_{q=O_a}^{O_a+Z_a-1} \sum_{w=-(N_b-1)}^{N_b-1} (N_b - |w|) \times e^{-\pi|w|\Omega_b T_{\text{samp}}} \tilde{r}^{(b)}[w] e^{j\frac{2\pi}{N_a}(q-2^\mu p)(w)}. \tag{25}$$

Proof: The proof is given in Appendix B. ∎

Result 2 shows that $\mathbf{K}_{\text{INI}}^{(b)}(p, \mathbf{Q}^{(a)}) \propto \mathbf{R}^{(b)}$. However, the expressions for $\gamma_{\text{INI}}^{(b,a)}(p)$ and $\gamma_{\text{INI}}^{(a,b)}(p)$ are quite different. One manifestation of this is that the INI covariance at user b does not depend upon the powers $r_0^{(b)}[0], r_1^{(b)}[0], \ldots, r_{L-1}^{(b)}[0]$ of the channel taps. On the other hand, the INI at user a does depend on $r_0^{(a)}[0], r_1^{(a)}[0], \ldots, r_{L-1}^{(a)}[0]$.

The total INI covariance on user k in (13) can be computed using Results 1 and 2 as follows. In the summation in (13), for $l < k$, $\mathbf{K}_{\text{INI}}^{(k)}(p, \mathbf{Q}^{(l)})$ is computed by substituting $b = k$ and $a = l$ in (24). When $l > k$, it is computed by substituting $a = k$ and $b = l$ in (22).

B. ICI Analysis

Result *3:* The covariance matrix $\mathbf{K}_{\text{ICI}}^{(k)}(p, \mathbf{Q}^{(k)})$ of the ICI at subcarrier p of any user k is given by

$$\mathbf{K}_{\text{ICI}}^{(k)}(p, \mathbf{Q}^{(k)}) = \gamma_{\text{ICI}}^{(k)}(p) \left\langle \mathbf{Q}^{(k)}, \mathbf{T}^{(k)} \right\rangle \mathbf{R}^{(k)}, \tag{26}$$

where

$$\gamma_{\text{ICI}}^{(k)}(p) \triangleq \frac{\beta_k}{N_k Z_k M_t} \sum_{q=O_k, q\neq p}^{O_k+Z_k-1} \Bigg[\sum_{w=-(N_k-1)}^{N_k-1} (N_k - |w|) \times e^{-\pi|w|\Omega_k T_{\text{samp}}} \tilde{r}^{(k)}[w] e^{j\frac{2\pi}{N_k}(q-p)w} \Bigg]. \tag{27}$$

Proof: The proof is given in Appendix C. ∎

We see that $\mathbf{K}_{\text{ICI}}^{(k)}(p, \mathbf{Q}^{(k)}) \propto \mathbf{R}^{(k)}$. A subtle point to note is that the scaling constant $\gamma_{\text{ICI}}^{(k)}(p)$ is, in general, a function of the subcarrier index p. Only when all the subcarriers are occupied ($Z_k = N_k$ and $O_k = 0$), does $\gamma_{\text{ICI}}^{(k)}(p)$ become the same for all subcarriers. In this case, (27) simplifies to

$$\gamma_{\text{ICI}}^{(k)}(p) = \gamma_{\text{ICI}}^{(k)}(0) = \frac{\beta_k}{N_k^2 M_t} \sum_{q=1}^{N_k-1} \sum_{w=-(N_k-1)}^{N_k-1} (N_k - |w|) \times e^{-\pi|w|\Omega_k T_{\text{samp}}} \tilde{r}^{(k)}[w] e^{j\frac{2\pi}{N_k}qw}, \ \forall p. \tag{28}$$

IV. Optimal Transmit Precoder

We now derive the optimal precoder for each user that maximizes its ergodic capacity given the other users' precoders.[1] The ergodic rate $C^{(k)}\left(p, \mathbf{Q}^{(k)}, \mathbf{Q}^{(\backslash k)}\right)$ of user k on subcarrier p can be written as the following difference of two terms [41]:

$$C^{(k)}\left(p, \mathbf{Q}^{(k)}, \mathbf{Q}^{(\backslash k)}\right) = \mathbb{E}\Big[\log_2 \Big(\det \Big[\sigma^2 \mathbf{I}_{M_r} + \mathbf{K}_{\text{ICI}}^{(k)}(p, \mathbf{Q}^{(k)}) + \overline{\mathbf{K}}_{\text{INI}}^{(k)}(p) + \mathbf{G}^{(k,k)}(p,m,p,m) \mathbf{Q}^{(k)} \mathbf{G}^{(k,k)\dagger}(p,m,p,m) \Big] / \det \Big[\sigma^2 \mathbf{I}_{M_r} + \mathbf{K}_{\text{ICI}}^{(k)}(p, \mathbf{Q}^{(k)}) + \overline{\mathbf{K}}_{\text{INI}}^{(k)}(p) \Big] \Big) \Big]. \tag{29}$$

Here, the expectation is over $\mathbf{G}^{(k,k)}(p,m,p,m)$, which is a function of the MIMO channel from the BS to user k. Using the linearity of expectation, we get

$$C^{(k)}\left(p, \mathbf{Q}^{(k)}, \mathbf{Q}^{(\backslash k)}\right) = C_S^{(k)}\Big(p, \mathbf{Q}^{(k)}, \mathbf{Q}^{(\backslash k)}\Big) - C_I^{(k)}\Big(p, \mathbf{Q}^{(k)}, \mathbf{Q}^{(\backslash k)}\Big), \tag{30}$$

[1]By definition, the ergodic capacity is the supremum of the rates achieved by all possible transmit and receive architectures.

where

$$C_S^{(k)}\Big(p,\mathbf{Q}^{(k)},\mathbf{Q}^{(\backslash k)}\Big) = \mathbb{E}\Big[\log_2\Big(\det\Big[\sigma^2\mathbf{I}_{M_r}+\mathbf{K}_{\text{ICI}}^{(k)}(p,\mathbf{Q}^{(k)})+\overline{\mathbf{K}}_{\text{INI}}^{(k)}(p) + \mathbf{G}^{(k,k)}(p,m,p,m)\mathbf{Q}^{(k)}\mathbf{G}^{(k,k)\dagger}(p,m,p,m)\Big]\Big)\Big], \quad (31)$$

and

$$C_I^{(k)}\Big(p,\mathbf{Q}^{(k)},\mathbf{Q}^{(\backslash k)}\Big) = \log_2\Big(\det\Big[\sigma^2\mathbf{I}_{M_r}+\mathbf{K}_{\text{ICI}}^{(k)}(p,\mathbf{Q}^{(k)})+\overline{\mathbf{K}}_{\text{INI}}^{(k)}(p)\Big]\Big). \quad (32)$$

The above expression is different from the expression in [10], which does not consider INI and ICI. Notice that the expression for $C_I^{(k)}\big(p,\mathbf{Q}^{(k)},\mathbf{Q}^{(\backslash k)}\big)$ does not have an expectation.

The ergodic capacity of user k on subcarrier p is the solution of the following optimization problem $\mathcal{P}$:

$$\mathcal{P}: \max_{\mathbf{Q}^{(k)}} \quad C^{(k)}\left(p,\mathbf{Q}^{(k)},\mathbf{Q}^{(\backslash k)}\right), \quad (33)$$

$$\text{s.t.} \quad \mathbf{Q}^{(k)} \succeq \mathbf{0}, \quad (34)$$

$$\text{Tr}\left\{\mathbf{Q}^{(k)}\right\} \leq P_{\max}^{(k)}. \quad (35)$$

The constraint in (34) arises because $\mathbf{Q}^{(k)}$ is a covariance matrix and must, therefore, be positive semi-definite. And, (35) constrains the transmit power per subcarrier to be less than or equal to $P_{\max}^{(k)}$. The solution of $\mathcal{P}$ is as follows.

Result *4:* For any given power allocation $\left\{\mathbf{P}^{(i)}\right\}_{i=1}^{K}$ and precoders $\{\mathbf{F}_i\}_{i=1,i\neq k}^{K}$, the optimal precoder $\mathbf{F}_k^{\text{opt}}$ for any subcarrier of user k is the matrix of eigenvectors of the transmit spatial correlation $\mathbf{T}^{(k)}$ of the channel of user k:

$$\mathbf{F}_k^{\text{opt}} = \mathbf{U}_T^{(k)}. \quad (36)$$

Proof: The proof is given in Appendix D. ■

We shall refer to the columns of $\mathbf{U}_T^{(k)}$ as the *statistical or spatial eigenmodes* of user k. Thus, each column of $\mathbf{U}_T^{(k)}$ carries one information symbol of the vector $\mathbf{s}^{(k)}[u,v]$.

A. Power Allocation

Given the precoders, we now determine the optimal power allocation matrices of the users that maximize the weighted sum rate of the mixed-numerology MIMO-OFDM system. The weighted sum rate $\bar{C}\left(\mathbf{Q}^{(1)},\ldots,\mathbf{Q}^{(K)}\right)$ is given by

$$\bar{C}\left(\mathbf{Q}^{(1)},\ldots,\mathbf{Q}^{(K)}\right) = \sum_{k=1}^{K} w_k \sum_{p=O_k}^{O_k+Z_k-1} C^{(k)}\left(p,\mathbf{Q}^{(k)},\mathbf{Q}^{(\backslash k)}\right), \quad (37)$$

where $w_k > 0$ are the weights. Assigning different weights to the users enables the BS to ensure user fairness [42, Ch. 2]. Typically, a cell-edge user with a weaker channel is assigned a larger weight so that its rate is prioritized more by the BS.

From Result 4, $\mathbf{Q}^{(k)} = \mathbf{U}_T^{(k)}\mathbf{P}^{(k)}\mathbf{U}_T^{(k)\dagger}$. The constrained optimization problem can be stated as[2]

$$\max_{\left\{\mathbf{P}^{(k)}\right\}_{k=1}^{K}} \quad \sum_{k=1}^{K} w_k \sum_{p=O_k}^{O_k+Z_k-1} C^{(k)}\left(p,\mathbf{Q}^{(k)},\mathbf{Q}^{(\backslash k)}\right), \quad (38)$$

$$\text{s.t.} \quad \sum_{k=1}^{K} Z_k \text{Tr}\left\{\mathbf{P}^{(k)}\right\} \leq P_{\max}, \quad (39)$$

$$\mathbf{P}^{(k)} \succeq \mathbf{0}, \ \forall k \in \{1,2,\ldots,K\}. \quad (40)$$

Recall that $\mathbf{Q}^{(\backslash k)}$ corresponds to $\left\{\mathbf{Q}^{(l)}\right\}_{l=1,l\neq k}^{K}$. The constraint (39) limits the total transmit power of the BS on all subcarriers to $P_{\max}$, and the constraint (40) follows from (34).

From (30), the objective function in (38) becomes

$$\left[\sum_{k=1}^{K} w_k \sum_{p=O_k}^{O_k+Z_k-1} C_S^{(k)}\Big(p,\mathbf{Q}^{(k)},\mathbf{Q}^{(\backslash k)}\Big)\right] - \left[\sum_{k=1}^{K} w_k \sum_{p=O_k}^{O_k+Z_k-1} C_I^{(k)}\Big(p,\mathbf{Q}^{(k)},\mathbf{Q}^{(\backslash k)}\Big)\right]. \quad (41)$$

Each function above within the square brackets is a concave function. Hence, the expression in (41) is a difference of two concave functions. Thus, the optimization problem is non-convex. We use the SCA approach to determine the optimal power allocation as follows. In the t^{th} iteration, we replace the second concave function of the objective function in (41) with the following first-order approximation $f_{t-1}\left(\mathbf{P}^{(1)},\ldots,\mathbf{P}^{(K)}\right)$ about the point $\left(\mathbf{P}_{t-1}^{(1)},\ldots,\mathbf{P}_{t-1}^{(K)}\right)$:

$$f_{t-1}\left(\mathbf{P}^{(1)},\ldots,\mathbf{P}^{(K)}\right) \triangleq \sum_{k=1}^{K} w_k \times \sum_{p=O_k}^{O_k+Z_k-1}\left[C_I^{(k)}\Big(p,\mathbf{Q}_{t-1}^{(k)},\mathbf{Q}_{t-1}^{(\backslash k)}\Big) + \sum_{j=1}^{K}\left\langle\nabla_{\mathbf{P}^{(j)}} C_I^{(k)}\Big(p,\mathbf{Q}_{t-1}^{(k)},\mathbf{Q}_{t-1}^{(\backslash k)}\Big),\mathbf{P}^{(j)}-\mathbf{P}_{t-1}^{(k)}\right\rangle\right]. \quad (42)$$

Here, $\mathbf{Q}_{t-1}^{(k)} = \mathbf{U}_T^{(k)}\mathbf{P}_{t-1}^{(k)}\mathbf{U}_T^{(k)\dagger}$ and $\mathbf{Q}_{t-1}^{(\backslash k)} = \left\{\mathbf{Q}_{t-1}^{(l)}\right\}_{l=1,l\neq k}^{K}$. Appendix E contains the closed-form expressions for the gradients. We then obtain the following relaxed convex optimization problem $\mathcal{P}_t$:

$$\mathcal{P}_t: \quad \max_{\left\{\mathbf{P}^{(k)}\right\}_{k=1}^{K}} \sum_{k=1}^{K} w_k \sum_{p=O_k}^{O_k+Z_k-1} C_S^{(k)}\Big(p,\mathbf{Q}^{(k)},\mathbf{Q}^{(\backslash k)}\Big) - f_{t-1}\left(\mathbf{P}^{(1)},\ldots,\mathbf{P}^{(K)}\right), \quad (43)$$

$$\text{s.t.} \quad \sum_{k=1}^{K} Z_k \text{Tr}\left\{\mathbf{P}^{(k)}\right\} \leq P_{\max}, \quad (44)$$

$$\mathbf{P}^{(k)} \succeq \mathbf{0}, \forall k \in \{1,2,\ldots,K\}. \quad (45)$$

Let the solution of $\mathcal{P}_t$ be $\left(\mathbf{P}_t^{(1)},\ldots,\mathbf{P}_t^{(K)}\right)$. It can be

[2]A more general problem is to jointly optimize the powers and the precoding matrices. However, this problem is intractable because the sum rate of each user is a function of $\left\{\mathbf{Q}^{(k)}\right\}_{k=0}^{K-1}$. Due to this, the weighted sum rate objective function is no longer a separable function of $\left\{\mathbf{P}^{(k)}\right\}_{k=0}^{K-1}$.

found by standard tools such as CVX and Matlab. Note that the function $C_S^{(k)}(\cdot,\cdot,\cdot)$ in (31) is in terms of an expectation of a determinant. Given the involved form of the terms inside the determinant, no closed-form expression for the expectation exists. Therefore, we compute it by taking an empirical average generated from T independent and identically distributed (i.i.d.) random channel realizations.[3] Thus, we generate a sequence of solutions $\left\{\left(\mathbf{P}_0^{(1)},\ldots,\mathbf{P}_0^{(K)}\right),\ldots,\left(\mathbf{P}_t^{(1)},\ldots,\mathbf{P}_t^{(K)}\right),\ldots\right\}$.

The constraint set of $\mathcal{P}_t$ is compact. Furthermore, the sequence of values of the objective function is monotonically non-decreasing. Therefore, our algorithm provably converges to a local maximum $\left(\mathbf{P}_*^{(1)},\ldots,\mathbf{P}_*^{(K)}\right)$ [43].

Algorithm 1 shows the procedure to obtain the power allocation.

Complexity: Let N_{it} be the iterations used to solve the convex problem $\mathcal{P}_t$ through sequential quadratic programming approach. The complexity of computing the Hessian is $\mathcal{O}\left(TK\left(KM_t\right)^2\right)$ and that of solving a quadratic program is $\mathcal{O}\left(\left(KM_t\right)^3\right)$. Thus, the computational complexity for an SCA iteration is $\mathcal{O}\left(TK^3M_t^2+N_{\text{it}}K^3M_t^3\right)$.

Algorithm 1: Power allocation

1 Initialize iteration counter $t=0$ and tolerance to ϵ.
2 $\mathbf{P}_0^{(k)}=P_{\max}\mathbf{I}_{M_t}/(KZ_kM_t),\ \forall k\in\{1,2,\ldots,K\}$.
3 **repeat**
4 Calculate $C_S^{(k)}\left(p,\mathbf{Q}^{(k)},\mathbf{Q}^{(\backslash k)}\right)$ by taking an empirical average from T i.i.d. channel realizations.
5 Solve the convex optimization problem $\mathcal{P}_t$ in (43) to obtain $\left(\mathbf{P}_t^{(1)},\ldots,\mathbf{P}_t^{(K)}\right)$.
6 $t\leftarrow t+1$
7 **until** $\left|\bar{C}\left(\mathbf{Q}_t^{(1)},\ldots,\mathbf{Q}_t^{(K)}\right)-\bar{C}\left(\mathbf{Q}_{t-1}^{(1)},\ldots,\mathbf{Q}_{t-1}^{(K)}\right)\right|\le\epsilon$
8 return $\left(\mathbf{P}_*^{(1)},\ldots,\mathbf{P}_*^{(K)}\right)=\left(\mathbf{P}_t^{(1)},\ldots,\mathbf{P}_t^{(K)}\right)$.

V. Numerical Results

We now present Monte Carlo simulation results to quantitatively understand the behavior of the INI and ICI covariances, the weighted sum rate, and the power allocation.

Simulation Settings: We consider a BS and three users with three numerologies. As mentioned earlier, no more than three numerologies can be used in a frequency range in 5G NR even with more users. Each user is equipped with a half-wavelength spaced antenna linear array and a Laplacian PAS [25]. Unless mentioned otherwise, $M_t=M_r=4$. We use the TDL-C channel model, which is one of the test models adopted by 3GPP [25]. The delay spread is 100 ns. The MIMO and OFDM parameters are given in Table II.

Each user is allocated 12 subcarriers. User 1, which uses the base numerology, occupies subcarriers 0 to 11. User 2 occupies subcarriers 7 to 18 as per its numerology 1, which correspond to subcarriers 13 to 37 in the base numerology. User 3 occupies subcarriers 10 to 21 as per its numerology 2, which correspond to subcarriers 38 to 86 in the base numerology. Notice that the subcarriers are partially occupied and there are guard bands between the subcarriers assigned to the users. Fig. 2 illustrates the subcarrier allocations. The indices shown at the top indicate the subcarrier indices of the users specific to their numerologies, while the indices shown at the bottom represent the subcarrier indices with respect to the base numerology. The sampling rate is 7.68 MHz. The expectation in (31) is computed as an empirical average of 10000 independent channel realizations.

[3]We cannot use deterministic equivalents to avoid averaging because we are not operating in the massive MIMO regime with a large number of transmit antennas.

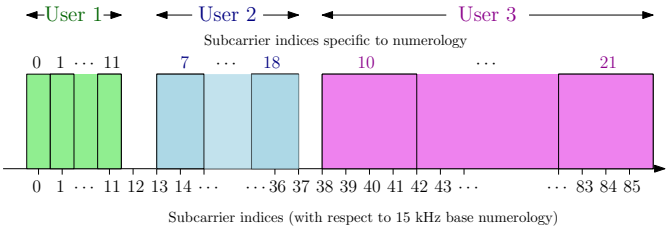

Fig. 2. Subcarrier locations of the users.

TABLE II
Simulation Parameters

Parameter	*User* 1	*User* 2	*User* 3
Numerology (ℓ_k)	0	1	2
DFT length (N_k)	512	256	128
Number of subcarriers (Z_k)	12	12	12
Offset (O_k)	0	7	10
Subcarrier spacing ($b^{(k)}$)	15 kHz	30 kHz	60 kHz
OFDM symbol duration ($T_s^{(k)}$)	66.67 μs	33.33 μs	16.66 μs
AoD mean ($m_t^{(k)}$)	45°	20°	30°
AoD standard deviation ($s_t^{(k)}$)	15°	30°	20°
AoA mean ($m_r^{(k)}$)	45°	20°	30°
AoA standard deviation ($s_r^{(k)}$)	15°	30°	20°

A. INI and ICI Powers

Fig. 3 plots the normalized total INI power (summed over the antennas) at each subcarrier when $\mathbf{Q}^{(k)}=\mathbf{I}_4,\forall k$, for equal power allocation (EPA). Specifically, it plots $\text{Tr}\left\{\overline{\mathbf{K}}_{\text{INI}}^{(k)}(p)\right\}/\left(\beta_k\mathsf{EP}_k\right)$, for $k=1,2$. This ratio measures the INI power relative to the EPRE. Since it is a dimensionless quantity, its units are in dB. Also shown is the INI power contributed by each of the other users. Figs. 3(a) and 3(b) show the results for users 1 and 2, respectively. The INI power exhibits a wide dynamic range of 9.7 dB across the subcarriers for user 1 and 7.6 dB for user 2. We observe that user 2 experiences a higher INI power at its edge subcarriers than at its middle subcarriers, due to interference from user 1 on the left and user 3 on the right. For user 1, the right edge subcarriers face more INI from the nearby interfering users. At user 1, the INI powers caused by users 2 and 3 are both oscillatory in nature. In contrast, at user 2, the INI power caused by user 3 is oscillatory, while that caused by user 1 is monotonic. The oscillatory behavior of the INI follows from

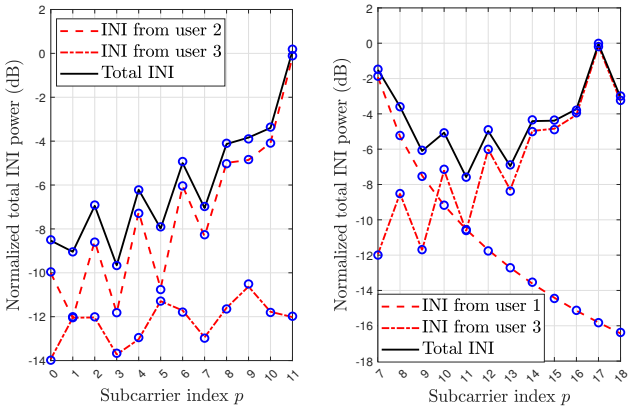

(a) User 1 (b) User 2

Fig. 3. Normalized total INI power as a function of the subcarrier index ($\beta_1 = \beta_3 = -3$ dB, $\beta_2 = -1$ dB, $f_d^{(1)} = 500$ Hz, $f_d^{(2)} = f_d^{(3)} = 600$ Hz, and $\Omega_1 = \Omega_2 = \Omega_3 = 50$ Hz). Simulation results are shown using the marker 'o', and analysis results are shown using lines.

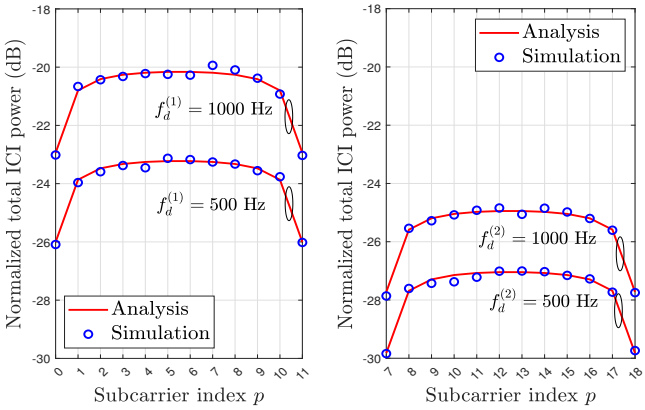

(a) User 1 (b) User 2

Fig. 4. Normalized total ICI power as a function of the subcarrier index ($\beta_1 = \beta_3 = -3$ dB, $\beta_2 = -1$ dB, and $\Omega_1 = \Omega_2 = \Omega_3 = 50$ Hz).

the form of (23). It has the form of the DFT of a decreasing ramp function that is evaluated at multiples of $b^{(1)}$, $b^{(2)}$, and $b^{(3)}$. This can be shown to cause the oscillations. The analysis and simulation results match each other well. The trends for user 3 are similar to that of user 1 except that its left edge subcarriers face more INI from both users 1 and 2. Its plot is not shown to conserve space.

Fig. 4 plots the total normalized ICI power, summed over all the antennas, at each subcarrier when $\mathbf{Q}^{(k)} = \mathbf{I}_4, \forall k$ for EPA. It plots $\mathrm{Tr}\left\{\mathbf{K}_{\mathrm{ICI}}^{(k)}(p, \mathbf{I}_4)\right\} / (\beta_k \mathsf{EP}_k)$ as a function of the subcarrier index for two Doppler spreads. Figs. 4(a) and 4(b) show the results for users 1 and 2, respectively. The precoder $\mathbf{U}_T^{(k)}$ is used with EPA. For both users, the ICI power remains relatively flat across subcarriers, except for the edge subcarriers. The ICI power at the edge subcarriers is 2 dB lower than that at the central subcarriers. This is because the contribution of the adjacent subcarriers in the total ICI power is larger. Thus, the ICI power has a smaller dynamic range compared to INI power. The total ICI power for user 2 is 3.8 dB lower than that of user 1. This is because the subcarrier spacing of user 2 is twice that of user 1. The trends are similar for user 3, whose plot is not shown to avoid clutter. Its total ICI power is 3.5 dB lower than that of user 2. We also observe that the INI and ICI powers at the edge subcarriers exhibit qualitatively different trends.

B. Weighted Sum Rate: Benchmarking and Trends

We benchmark our method with the following:

- *INI and ICI-Unaware Power Allocation (I^2UPA) [10]:* The precoder for user k is $\mathbf{U}_T^{(k)}$. The power allocation is obtained from the convex optimization-based method of [10]. This comparison is instructive as it brings out the impact of INI and ICI. We also present this comparison given the seminal nature of the result in [10] on statistical CSI-based precoding, which is also employed in recent works such as [44]–[46].
- *DFT Precoder with INI and ICI-Aware Power Allocation (DFT-I^2APA):* The precoder for all the users is the DFT matrix of size M_t. The power allocation is obtained by numerically maximizing the weighted sum rate. This comparison brings out the impact of the precoder.
- *EPA:* In this method, all the eigenmodes are assigned equal power. As a result, $\mathbf{Q}^{(k)} \propto \mathbf{I}_{M_t}$ for any unitary precoder. Hence, we do not need to specify the precoder for EPA. This comparison brings out the impact of the power allocation.
- *Singular Value Decomposition (SVD)-based Method:* This method employs the SVD-based precoder and the water-filling power allocation. It ignores INI and ICI. This comparison brings out the impact of INI, ICI, and the precoder.
- *Strongest Eigenmode Method:* In this method, the transmitter assigns all the available power to the statistical eigenmode with the largest eigenvalue. This comparison brings out the impact of power allocation.
- *ZF Precoder [5]:* In this method, a ZF precoder, which uses instantaneous CSI, is employed to mitigate the INI. This comparison brings out the impact of the precoder.

We note that a comparison with the scheme in [18] is not possible since it focuses on receiver-side mitigation. And, no transmit power constraint is imposed in the INI pre-cancellation technique proposed in [19]; as a result, a fair comparison is challenging. A comparison with the works in [4], [6], [26], [27], [31] is not possible because they all focus on SISO.

Fig. 5 plots the weighted sum rate of the proposed power allocation method as a function of the scaled Doppler spread $f_d^{(1)} T_s^{(1)}$. We set $w_1 = w_3 = 0.4$ and $w_2 = 0.2$ to illustrate that users 1 and 3 can be given a higher preference than user 2. The results are shown for $\Omega_1 = \Omega_2 = \Omega_3 = 100$ Hz and $\Omega_1 = \Omega_2 = \Omega_3 = 300$ Hz. The Doppler spread of users 2 and 3 is equal to that of user 1. We see that the weighted sum rate decreases when $f_d^{(1)} T_s^{(1)}$ increases. When $f_d^{(1)} T_s^{(1)} = 0$, the weighted sum rate is 3.29 bps/Hz for $\Omega_1 = \Omega_2 = \Omega_3 =$

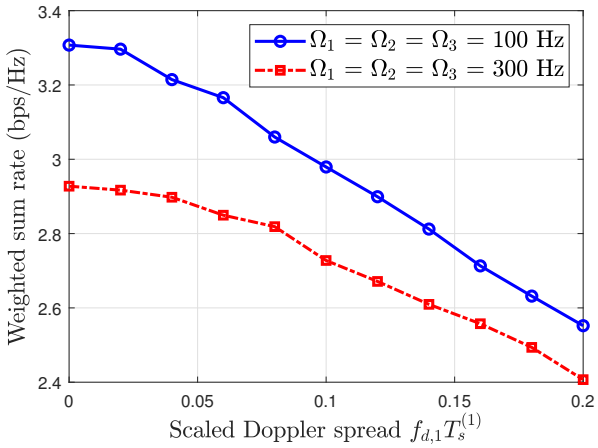

Fig. 5. Zoomed-in view of weighted sum rate as a function of the scaled Doppler spread ($w_1 = w_3 = 0.4$, $w_2 = 0.2$, $\beta_1 = \beta_3 = -3$ dB, $\beta_2 = -1$ dB, $P_{\max}/\sigma^2 = 20$ dB).

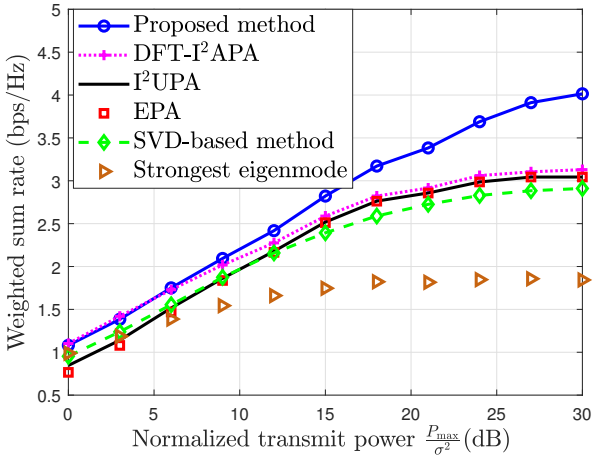

Fig. 6. Zoomed-in view of weighted sum rate as a function of the normalized transmit power ($w_1 = w_3 = 0.4$, $w_2 = 0.2$, $\beta_1 = \beta_3 = -3$ dB, $\beta_2 = -1$ dB, $f_d^{(1)} = 500$ Hz, $f_d^{(2)} = f_d^{(3)} = 600$ Hz, and $\Omega_1 = \Omega_2 = \Omega_3 = 150$ Hz).

100 Hz and is 2.92 bps/Hz for $\Omega_1 = \Omega_2 = \Omega_3 = 300$ Hz. This shows how the phase noise lowers the weighted sum rate.

Fig. 6 plots the weighted sum rate of the proposed power allocation method, DFT-I^{2}APA, I^{2}UPA, EPA, SVD-based method, and strongest eigenmode method as a function of the normalized transmit power $P_{\max}/\sigma^2$. The weighted sum rate of all the methods increases as $P_{\max}/\sigma^2$ increases. The proposed method has a higher weighted sum rate than the other methods at all powers. For example, when the normalized transmit power is 18 dB, the weighted sum rate of the proposed algorithm is 3.17 bps/Hz, while those of the DFT-I^{2}APA, I^{2}UPA, EPA, SVD-based, and the strongest eigenmode methods are 2.82, 2.762, 2.761, 2.58, and 1.82 bps/Hz, respectively. The gap between weighted sum rates of all other methods and the proposed method increases as $P_{\max}/\sigma^2$ increases. While I^{2}UPA achieves a higher weighted sum rate than EPA, the difference between the two is marginal due to INI and ICI. The strongest eigenmode method has the smallest weighted sum rate among all the methods, which shows the importance of using multiple eigenmodes.

To understand the above trends, Fig. 7 plots the fraction of the total power per subcarrier allocated to the eigenmodes of user 1 as a function of $P_{\max}/\sigma^2$. Recall that eigenmode i refers to the eigenvector associated with the i^{th} largest eigenvalue of $\mathbf{T}^{(1)}$. Fig. 7(a) plots the results for the proposed method and Fig. 7(b) plots the results for I^{2}UPA. Also shown is a horizontal line that corresponds to EPA. At low powers, the proposed method allocates the highest power to the strongest eigenmode. However, as $P_{\max}/\sigma^2$ increases, the power allocated to the eigenmode 1 decreases while the powers assigned to the other eigenmodes increase. On the other hand, I^{2}UPA always assigns the maximum power to the strongest eigenmode. As $P_{\max}$ increases, I^{2}UPA allocates the same power to all the eigenmodes unlike the proposed scheme.

We compare the weighted sum rates of the proposed method and the ZF precoder in Fig. 8. We show this comparison separately because the ZF precoder of [5] applies only to users with one receive antenna and requires that the number of transmit antennas is greater than or equal to the number of subcarriers per user. Even in a setup tailored for the ZF precoder, the proposed method achieves a higher weighted sum rate. For example, when the normalized transmit power is 9 dB, the weighted sum rate of the proposed algorithm is 2.65 bps/Hz while that of the ZF precoder is 1.68 bps/Hz.

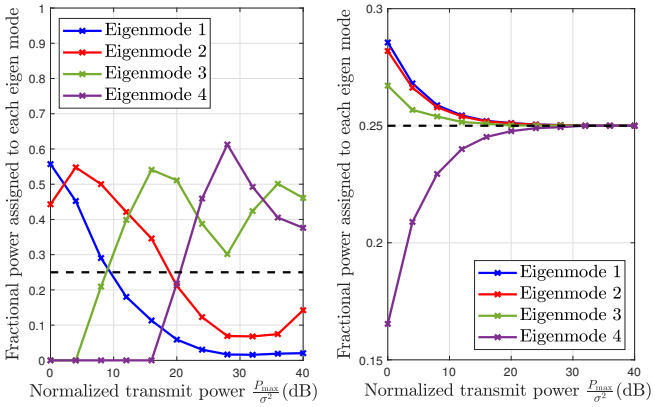

(a) Proposed method (b) I^{2}UPA

Fig. 7. Fractional power allocated to each eigenmode of user 1 as a function of the normalized transmit power ($w_1 = w_3 = 0.4$, $w_2 = 0.2$, $\beta_1 = \beta_3 = -3$ dB, $\beta_2 = -1$ dB, $f_d^{(1)} = 500$ Hz, $f_d^{(2)} = f_d^{(3)} = 600$ Hz, and $\Omega_1 = \Omega_2 = \Omega_3 = 150$ Hz).

Fig. 9 plots the weighted sum rate as a function of the number of iterations of the proposed algorithm. It shows results for different MIMO configurations. We observe that the algorithm converges within 30 iterations. The number of iterations required to converge is insensitive to the number of antennas.

Fig. 10 plots the weighted sum rate of the proposed power allocation method as a function of the standard deviation of the AoD $s_t^{(k)}$. It shows the results for different MIMO

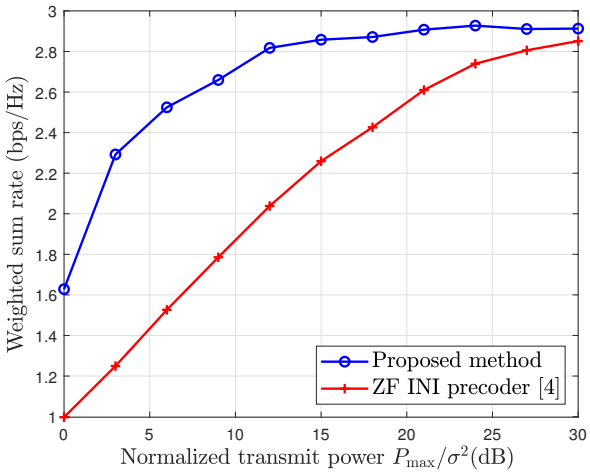

Fig. 8. Comparison of weighted sum rates of the zero-forcing precoder and the proposed scheme ($M_t = 4$, $M_r = 1$, $f_d^{(1)} = 500$ Hz, $f_d^{(2)} = 600$ Hz, $\Omega_1 = \Omega_2 = 150$ Hz, $O_1 = 0$, $O_2 = 3$, and $Z_1 = Z_2 = 2$).

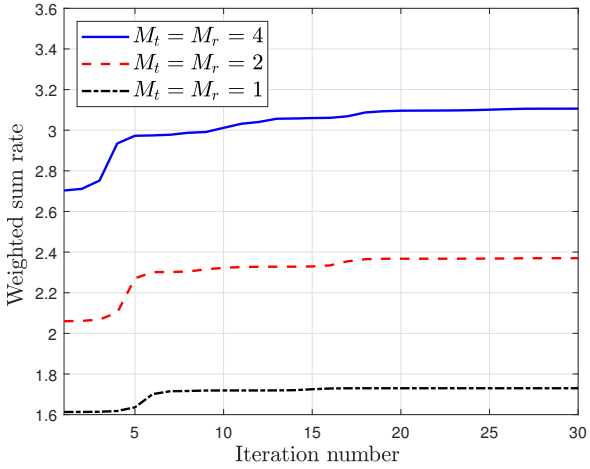

Fig. 9. Zoomed-in view of weighted sum rate as a function of the iteration number of the proposed algorithm ($w_1 = w_3 = 0.4$, $w_2 = 0.2$, $\beta_1 = \beta_3 = -3$ dB, $\beta_2 = -1$ dB, $P_{\max}/\sigma^2 = 20$ dB, $\Omega_1 = \Omega_2 = \Omega_3 = 100$ Hz, and $f_d^{(1)} = f_d^{(2)} = f_d^{(3)} = 1000$ Hz).

configuations and SISO. The larger the standard deviation, the less spatially correlated the channel. Hence, for all the MIMO configurations, the weighted sum rate increases as $s_t^{(k)}$ increases. The figure also shows the weighted sum rate in the absence of INI and ICI. We observe that INI and ICI have a more severe impact on the weighted sum rate as the number of antennas increases.

VI. Conclusions

We saw that the INI and ICI covariances were scaled versions of the receive spatial correlation matrix, while the scaling constant was a function of the temporal auto-correlation of the channel, the Doppler spread, the channel power delay profile, the effective phase noise auto-correlation, and the transmit spatial correlation matrix. We derived the precoder for each user that achieved the single-user ergodic

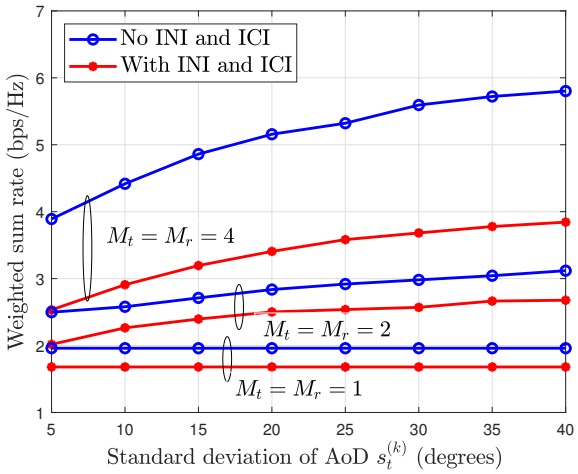

Fig. 10. Zoomed-in view of weighted sum rate as a function of the standard deviation of AoD ($w_1 = w_3 = 0.4$, $w_2 = 0.2$, $\beta_1 = \beta_3 = -3$ dB, $\beta_2 = -1$ dB, $f_d^{(1)} = 500$ Hz, $f_d^{(2)} = f_d^{(3)} = 600$ Hz, and $\Omega_1 = \Omega_2 = \Omega_3 = 150$ Hz).

capacity. It was the matrix of eigenvectors of the transmit spatial correlation matrix even for our more general model that considered INI and ICI. However, INI and ICI significantly altered the powers allocated to the spatial eigenmodes and led to lesser powers being assigned to the stronger eigenmodes at larger transmit powers. They made the power allocation problem non-convex. The proposed method achieved a higher weighted sum rate than several other approaches.

Analyzing the INI between OFDM and orthogonal time frequency space (OTFS), and for MIMO channel models more general than the Kronecker model, are avenues for future work. Another potential research direction is reducing the computational complexity of the algorithm. This can be achieved by developing analytically tractable bounds or approximations that forsake the need for Monte Carlo methods to compute the objective function. The above analytical form will also influence the number of iterations required by the algorithm to converge. Furthermore, characterizing the impact of imperfect synchronization and co-designing the transmit-receive architecture to better mitigate INI and ICI are open problems.

Acknowledgment

The authors would like to thank Dr. Chaveli Ramesh (Bharat Electronics Limited) for his support.

Appendix

A. Proof of Result 1

The INI covariance matrix $\mathbf{K}_{\text{INI}}^{(a)}(p, \mathbf{Q}^{(b)})$ for subcarrier p of user k due to user b is defined as

$$\mathbf{K}_{\text{INI}}^{(a)}(p, \mathbf{Q}^{(b)}) \triangleq \text{Cov}\left(\mathsf{INI}_a[p, m]\right). \tag{46}$$

Substituting (18) in (46), we get

$$\mathbf{K}_{\text{INI}}^{(a)}(p,\mathbf{Q}^{(b)}) = \text{Cov}\left[\sum_{v=0}^{2^\mu-1}\sum_{q=O_b}^{O_b+Z_b-1}\mathbf{G}^{(a,b)}(p,0,q,v)\bar{\mathbf{x}}^{(b)}[q,v]\right]. \quad (47)$$

Since $\bar{\mathbf{x}}^{(b)}[O_b,v], \bar{\mathbf{x}}^{(b)}[O_b+1,v], \ldots, \bar{\mathbf{x}}^{(b)}[O_b+Z_b-1,v]$ are independent, we get

$$\mathbf{K}_{\text{INI}}^{(a)}(p,\mathbf{Q}^{(b)}) = \sum_{v=0}^{2^\mu-1}\sum_{q=O_b}^{O_b+Z_b-1}\text{Cov}\left[\mathbf{G}^{(a,b)}(p,0,q,v)\bar{\mathbf{x}}^{(b)}[q,v]\right]. \quad (48)$$

Since $\bar{\mathbf{x}}^{(b)}[q,v]$ is zero-mean, we have

$$\text{Cov}\left[\mathbf{G}^{(a,b)}(p,0,q,v)\bar{\mathbf{x}}^{(b)}[q,v]\right] = \mathbb{E}\left[\mathbf{G}^{(a,b)}(p,0,q,v)\mathbf{Q}^{(b)}\mathbf{G}^{(a,b)\dagger}(p,0,q,v)\right]. \quad (49)$$

Hence, the $(i,j)^{\text{th}}$ element of $\mathbf{K}_{\text{INI}}^{(a)}(p,\mathbf{Q}^{(b)})$ is given by

$$\left[\mathbf{K}_{\text{INI}}^{(a)}(p,\mathbf{Q}^{(b)})\right]_{i,j} = \sum_{v=0}^{2^\mu-1}\sum_{q=O_b}^{O_b+Z_b-1}\left[\mathbb{E}\left[\mathbf{G}^{(a,b)}(p,0,q,v)\mathbf{Q}^{(b)}\mathbf{G}^{(a,b)\dagger}(p,0,q,v)\right]\right]_{i,j}. \quad (50)$$

Using the definition of matrix multiplication, we can show

$$\left[\mathbb{E}\left[\mathbf{G}^{(a,b)}(p,0,q,v)\mathbf{Q}^{(b)}\mathbf{G}^{(a,b)\dagger}(p,0,q,v)\right]\right]_{i,j} = \sum_{c=0}^{M_t-1}\sum_{d=0}^{M_t-1}\mathbb{E}\left[\mathbf{G}_{i,c}^{(a,b)}(p,0,q,v)\mathbf{G}_{j,d}^{(a,b)*}(p,0,q,v)\right]\times\mathbf{Q}_{c,d}^{(b)}. \quad (51)$$

Expression for $\mathbb{E}\left[\mathbf{G}_{i,c}^{(a,b)}(p,0,q,v)\mathbf{G}_{j,d}^{(a,b)*}(p,0,q,v)\right]$: We compute it separately for the three cases: $v=0$, $1\le v\le 2^\mu-2$, and $v=2^\mu-1$.

1) $v=0$*:* Substituting the expressions from (15) for $\mathbf{G}_{i,c}^{(a,b)}(p,0,q,0)$ and $\mathbf{G}_{j,d}^{(a,b)}(p,0,q,0)$ yields

$$\mathbb{E}\left[\mathbf{G}_{i,c}^{(a,b)}(p,0,q,0)\mathbf{G}_{j,d}^{(a,b)*}(p,0,q,0)\right] = \frac{\beta_a}{N_aZ_bM_t}\times\mathbb{E}\Bigg[\Bigg(\sum_{n_1=\text{CP}_a}^{N_b^T-1+l}\sum_{\tau_1=0}^{L-1}e^{j\phi_a[n_1]}h_{i,c}^{(a)}[n_1;\tau_1]\,e^{j\frac{2\pi}{N_a}(2^\mu q-p)n_1}\times e^{-j\frac{2\pi}{N_a}2^\mu q(\text{CP}_b+\tau_1)}e^{j\frac{2\pi}{N_a}p\text{CP}_a}\Bigg)\times\sum_{n_2=\text{CP}_a}^{N_b^T-1+l}\sum_{\tau_2=0}^{L-1}e^{-j\phi_a[n_2]}h_{j,d}^{(a)*}[n_2;\tau_2]\,e^{-j\frac{2\pi}{N_a}(2^\mu q-p)n_2}\times e^{j\frac{2\pi}{N_a}2^\mu q(\text{CP}_b+\tau_2)}e^{-j\frac{2\pi}{N_a}p\text{CP}_a}\Bigg]. \quad (52)$$

Using the linearity of expectation, we get

$$\mathbb{E}\left[\mathbf{G}_{i,c}^{(a,b)}(p,0,q,0)\mathbf{G}_{j,d}^{(a,b)*}(p,0,q,0)\right] = \frac{\beta_a}{N_aZ_bM_t}\times\sum_{n_1=\text{CP}_a}^{N_b^T-1+l}\sum_{\tau_1=0}^{L-1}\sum_{n_2=\text{CP}_a}^{N_b^T-1+l}\sum_{\tau_2=0}^{L-1}e^{j\frac{2\pi}{N_a}(2^\mu q-p)(n_1-n_2)}\times e^{-j\frac{2\pi}{N_a}2^\mu q(\tau_1-\tau_2)}\times\mathbb{E}\left[e^{j(\phi_a[n_1]-\phi_a[n_2])}h_{i,c}^{(a)}[n_1;\tau_1]\,h_{j,d}^{(a)*}[n_2;\tau_2]\right]. \quad (53)$$

The phase noise is independent of the channel tap gains. Moreover, $\forall\,\tau_1\neq\tau_2$, we have

$$\mathbb{E}\left[h_{i,c}^{(a)}[n_1;\tau_1]\,h_{j,d}^{(a)*}[n_2;\tau_2]\right] = 0, \quad (54)$$

because the channel coefficients corresponding to distinct delays are uncorrelated. Hence, (53) simplifies to

$$\mathbb{E}\left[\mathbf{G}_{i,c}^{(a,b)}(p,0,q,0)\mathbf{G}_{j,d}^{(a,b)*}(p,0,q,0)\right] = \frac{\beta_a}{N_aZ_bM_t}\times\sum_{\tau=0}^{L-1}\sum_{n_1=\text{CP}_a}^{N_b^T-1+\tau}\sum_{n_2=\text{CP}_a}^{N_b^T-1+\tau}e^{j\frac{2\pi}{N_a}(2^\mu q-p)(n_1-n_2)}\times\mathbb{E}\left[e^{j(\phi_a[n_1]-\phi_a[n_2])}\right]\mathbb{E}\left[h_{i,c}^{(a)}[n_1;\tau]\,h_{j,d}^{(a)*}[n_2;\tau]\right]. \quad (55)$$

From (6), we get

$$\mathbb{E}\left[e^{j(\phi_a[n_1]-\phi_a[n_2])}\right] = e^{-\pi|n_1-n_2|\Omega_aT_{\text{samp}}}. \quad (56)$$

Also, we know that

$$\mathbb{E}\left[h_{i,c}^{(a)}[n;\tau]\,h_{j,c}^{(a)*}[n;\tau]\right] = \mathbf{R}_{i,j}^{(a)}, \quad (57)$$

$$\mathbb{E}\left[h_{i,c}^{(a)}[n;\tau]\,h_{i,d}^{(a)*}[n;\tau]\right] = \mathbf{T}_{c,d}^{(a)*}, \quad (58)$$

$$\mathbb{E}\left[h_{i,c}^{(a)}[n_1;\tau]\,h_{i,c}^{(a)*}[n_2;\tau]\right] = r_\tau^{(a)}[n_1-n_2]. \quad (59)$$

Hence, (55) reduces to

$$\mathbb{E}\left[\mathbf{G}_{i,c}^{(a,b)}(p,0,q,0)\mathbf{G}_{j,d}^{(a,b)*}(p,0,q,0)\right] = \frac{\beta_a}{N_aZ_bM_t}\sum_{\tau=0}^{L-1}\sum_{n_1=\text{CP}_a}^{N_b^T-1+\tau}\sum_{n_2=\text{CP}_a}^{N_b^T-1+\tau}\mathbf{R}_{i,j}^{(a)}\mathbf{T}_{c,d}^{(a)*}\times r_\tau^{(a)}[n_1-n_2]\times e^{-\pi|n_1-n_2|\Omega_aT_{\text{samp}}}e^{j\frac{2\pi}{N_a}(2^\mu q-p)(n_1-n_2)}. \quad (60)$$

Substituting $M=N_b^T-\text{CP}_a$ and $w=n_1-n_2$ in (60), and enumerating the terms for each value of w, we get

$$\mathbb{E}\left[\mathbf{G}_{i,c}^{(a,b)}(p,0,q,0)\mathbf{G}_{j,d}^{(a,b)*}(p,0,q,0)\right] = \frac{\beta_a}{N_aZ_bM_t}\times\sum_{w=-(M+\tau-1)}^{M+\tau-1}\sum_{\tau=0}^{L-1}\mathbf{R}_{i,j}^{(a)}\mathbf{T}_{c,d}^{(a)*}(M+\tau-|w|)r_\tau^{(a)}[w]\times e^{-\pi|w|\Omega_aT_{\text{samp}}}e^{j\frac{2\pi}{N_a}(2^\mu q-p)w}. \quad (61)$$

2) $1 \leq v \leq 2^{\mu}-2$*:* Substituting the expressions for $\mathbf{G}_{i,c}^{(a,b)}(p,0,q,v)$ and $\mathbf{G}_{j,d}^{(a,b)}(p,0,q,v)$ from (15) yields

$$\mathbb{E}\left[\mathbf{G}_{i,c}^{(a,b)}(p,0,q,v)\mathbf{G}_{j,d}^{(a,b)*}(p,0,q,v)\right] = \frac{\beta_a}{N_a Z_b M_t} \times \mathbb{E}\Bigg[\Bigg(\sum_{\tau_1=0}^{L-1}\sum_{n_1=vN_b^T+\tau_1}^{(v+1)N_b^T+\tau_1} e^{j\phi_a[n_1]}h_{i,c}^{(a)}[n_1;\tau_1]\, e^{j\frac{2\pi}{N_a}(2^{\mu}q-p)n_1} \times e^{-j\frac{2\pi}{N_a}2^{\mu}q(\mathrm{CP}_b+vN_b^T+\tau_1)}e^{j\frac{2\pi}{N_a}p\mathrm{CP}_a}\Bigg) \times \sum_{\tau_2=0}^{L-1}\sum_{n_2=vN_b^T+\tau_2}^{(v+1)N_b^T+\tau_2} e^{-j\phi_a[n_2]}h_{j,d}^{(a)*}[n_2;\tau_2] \times e^{-j\frac{2\pi}{N_a}(2^{\mu}q-p)n_2}e^{j\frac{2\pi}{N_a}2^{\mu}q(\mathrm{CP}_b+vN_b^T+\tau_2)}e^{-j\frac{2\pi}{N_a}p\mathrm{CP}_a}\Bigg]. \quad (62)$$

Following the procedure in Appendix A1, we can show that

$$\mathbb{E}\left[\mathbf{G}_{i,c}^{(a,b)}(p,0,q,v)\mathbf{G}_{j,d}^{(a,b)*}(p,0,q,v)\right] = \frac{\beta_a}{N_a Z_b M_t} \times \sum_{\tau=0}^{L-1}\sum_{w=-(N_b^T-1)}^{N_b^T-1} \mathbf{R}_{i,j}^{(a)}\mathbf{T}_{c,d}^{(a)*}(N_b^T-|w|)r_{\tau}^{(a)}[w] \times e^{-\pi|w|\Omega_a T_{\mathrm{samp}}}e^{j\frac{2\pi}{N_a}(2^{\mu}q-p)w}. \quad (63)$$

3) $v = 2^{\mu}-1$*:* Substituting the expressions from (15) for $\mathbf{G}_{i,c}^{(a,b)}(p,0,q,2^{\mu}-1)$ and $\mathbf{G}_{j,d}^{(a,b)}(p,0,q,2^{\mu}-1)$ in (51) yields

$$\mathbb{E}\left[\mathbf{G}_{i,c}^{(a,b)}(p,0,q,2^{\mu}-1)\mathbf{G}_{j,d}^{(a,b)*}(p,0,q,2^{\mu}-1)\right] = \frac{\beta_a}{N_a Z_b M_t}\mathbb{E}\Bigg[\Bigg(\sum_{\tau_1=0}^{L-1}\sum_{n_1=(2^{\mu}-1)N_b^T+\tau_1}^{N_a^T} e^{j\phi_a[n_1]}h_{i,c}^{(a)}[n_1;\tau_1] \times e^{j\frac{2\pi}{N_a}(2^{\mu}q-p)n_1}e^{-j\frac{2\pi}{N_a}2^{\mu}q(\mathrm{CP}_b+(2^{\mu}-1)N_b^T+\tau_1)}e^{j\frac{2\pi}{N_a}p\mathrm{CP}_a}\Bigg) \times \sum_{\tau_2=0}^{L-1}\sum_{n_2=(2^{\mu}-1)N_b^T+\tau_2}^{N_a^T} e^{-j\phi_a[n_2]}h_{j,d}^{(a)*}[n_2;\tau_2] \times e^{-j\frac{2\pi}{N_a}(2^{\mu}q-p)n_2}e^{j\frac{2\pi}{N_a}2^{\mu}q(\mathrm{CP}_b+(2^{\mu}-1)N_b^T+\tau_2)}e^{-j\frac{2\pi}{N_a}p\mathrm{CP}_a}\Bigg]. \quad (64)$$

Following the procedure in Appendix A1, we get

$$\mathbb{E}\left[\mathbf{G}_{i,c}^{(a,b)}(p,0,q,2^{\mu}-1)\mathbf{G}_{j,d}^{(a,b)*}(p,0,q,2^{\mu}-1)\right] = \frac{\beta_a}{N_a Z_b M_t}\sum_{\tau=0}^{L-1}\sum_{w=-(N_b^T-\tau-1)}^{N_b^T-\tau-1} \mathbf{R}_{i,j}^{(a)}\mathbf{T}_{c,d}^{(a)*}(N_b^T-\tau-|w|) \times r_{\tau}^{(a)}[w]e^{-\pi|w|\Omega_a T_{\mathrm{samp}}}e^{j\frac{2\pi}{N_a}(2^{\mu}q-p)w}. \quad (65)$$

Substituting (61), (63), and (65) in (50) yields (22).

B. Brief Proof of Result 2

Substituting (21) in (46) and using the fact that $\bar{\mathbf{x}}^{(a)}[O_a,0], \bar{\mathbf{x}}^{(a)}[O_a+1,0], \ldots, \bar{\mathbf{x}}^{(a)}[O_a+Z_a-1,0]$ are independent, we get the following expression for any m:

$$\mathbf{K}_{\mathrm{INI}}^{(b)}(p,\mathbf{Q}^{(a)}) = \sum_{q=O_a}^{O_a+Z_a-1}\mathrm{Cov}\left[\mathbf{G}^{(b,a)}(p,m,q,0)\bar{\mathbf{x}}^{(a)}[q,0]\right]. \quad (66)$$

Furthermore, $\mathrm{Cov}\left[\mathbf{G}^{(b,a)}(p,m,q,0)\bar{\mathbf{x}}^{(a)}[q,0]\right] = \mathbb{E}\left[\mathbf{G}^{(b,a)}(p,m,q,0)\mathbf{Q}^{(a)}\mathbf{G}^{(b,a)\dagger}(p,m,q,0)\right]$. Thus, the $(i,j)^{\mathrm{th}}$ element of $\mathbf{K}_{\mathrm{INI}}^{(b)}(p,\mathbf{Q}^{(a)})$ is given by

$$\left[\mathbf{K}_{\mathrm{INI}}^{(b)}(p,\mathbf{Q}^{(a)})\right]_{i,j} = \sum_{q=O_a}^{O_a+Z_a-1}\left[\mathbb{E}\left[\mathbf{G}^{(b,a)}(p,m,q,0)\mathbf{Q}^{(a)}\mathbf{G}^{(b,a)\dagger}(p,m,q,0)\right]\right]_{i,j}. \quad (67)$$

Similar to (51), we can show that the $(i,j)^{\mathrm{th}}$ element of $\mathbb{E}\left[\mathbf{G}^{(b,a)}(p,m,q,0)\mathbf{Q}^{(a)}\mathbf{G}^{(b,a)\dagger}(p,m,q,0)\right]$ is

$$\left[\mathbb{E}\left[\mathbf{G}^{(b,a)}(p,m,q,0)\mathbf{Q}^{(a)}\mathbf{G}^{(b,a)\dagger}(p,m,q,0)\right]\right]_{i,j} = \sum_{c=0}^{M_t-1}\sum_{d=0}^{M_t-1}\mathbb{E}\left[\mathbf{G}_{i,c}^{(b,a)}(p,m,q,0)\mathbf{G}_{j,d}^{(b,a)*}(p,m,q,0)\right]\mathbf{Q}_{c,d}^{(a)}. \quad (68)$$

Upon substituting the expressions for $\mathbf{G}_{i,c}^{(b,a)}(p,m,q,0)$ and $\mathbf{G}_{j,d}^{(b,a)}(p,m,q,0)$ from (15), the expectation term in the right side of (68) becomes

$$\mathbb{E}\left[\mathbf{G}_{i,c}^{(b,a)}(p,m,q,0)\mathbf{G}_{j,d}^{(b,a)*}(p,m,q,0)\right] = \frac{\beta_b}{Z_a N_b M_t} \times \mathbb{E}\Bigg[\Bigg(\sum_{n_1=mN_b^T+\mathrm{CP}_b}^{(m+1)N_b^T-1}\sum_{\tau_1=0}^{L-1} e^{j\phi_b[n_1]}h_{i,c}^{(b)}[n_1;\tau_1]\, e^{j\frac{2\pi}{N_a}(q-2^{\mu}p)n_1} \times e^{-j\frac{2\pi}{N_a}q(\mathrm{CP}_a+\tau_1)}e^{j\frac{2\pi}{N_2}p(mN_b^T+\mathrm{CP}_b)}\Bigg) \times \sum_{n_2=mN_b^T+\mathrm{CP}_b}^{(m+1)N_b^T-1}\sum_{\tau_2=0}^{L-1} e^{-j\phi_b[n_2]}h_{j,d}^{(b)*}[n_2;\tau_2]\, e^{-j\frac{2\pi}{N_a}(q-2^{\mu}p)n_2} \times e^{j\frac{2\pi}{N_a}q(\mathrm{CP}_a+\tau_2)}e^{-j\frac{2\pi}{N_2}p(mN_b^T+\mathrm{CP}_b)}\Bigg]. \quad (69)$$

Following the procedure in Appendix A1, we get

$$\left[\mathbb{E}\left[\mathbf{G}^{(b,a)}(p,m,q,0)\mathbf{Q}^{(a)}\mathbf{G}^{(b,a)\dagger}(p,m,q,0)\right]\right]_{i,j} = \frac{\beta_b}{Z_a N_b M_t}\sum_{\tau=0}^{L-1}\sum_{w=-(N_b-1)}^{N_b-1}\mathbf{R}_{i,j}^{(b)}e^{-\pi|w|\Omega_b T_{\mathrm{samp}}} \times (N_b-|w|)r_{\tau}^{(b)}[w]e^{j\frac{2\pi}{N_a}(q-2^{\mu}p)w}\left\langle\mathbf{Q}^{(a)},\mathbf{T}^{(b)}\right\rangle. \quad (70)$$

Substituting $r_{\tau}^{(b)}[w] = r_{\tau}^{(b)}[0]\tilde{r}^{(b)}[w]$ and $\sum_{\tau=0}^{L-1}r_{\tau}^{(b)}[0]=1$ in (70), and then substituting the result in (67) yields (24).

C. Brief Proof of Result 3

The ICI covariance matrix $\mathbf{K}_{\mathrm{ICI}}^{(k)}(p,\mathbf{Q}^{(k)})$ for subcarrier p of user k is defined as

$$\mathbf{K}_{\mathrm{ICI}}^{(k)}(p,\mathbf{Q}^{(k)}) \triangleq \mathrm{Cov}\left(\mathsf{ICI}_k[p,m]\right). \quad (71)$$

Substituting $a = k$ in (17), and then in (71), and following a procedure similar to Appendices A and B, we can show that

$$\left[\mathbf{K}_{\text{ICI}}^{(k)}(p,\mathbf{Q}^{(k)})\right]_{i,j} = \sum_{c=0}^{M_t-1}\sum_{d=0}^{M_t-1}\mathbf{Q}_{c,d}^{(k)} \times \mathbb{E}\left[\mathbf{G}_{i,c}^{(k,k)}(p,m,q,m)\mathbf{G}_{j,d}^{(k,k)*}(p,m,q,m)\right]. \quad (72)$$

Proceeding along the lines of Appendices A and B, the expectation term in (72) is given by

$$\mathbb{E}\left[\mathbf{G}_{i,c}^{(k,k)}(p,m,q,m)\mathbf{G}_{j,d}^{(k,k)*}(p,m,q,m)\right] = \frac{\beta_k}{N_k Z_k M_t}\mathbf{R}_{i,j}^{(k)}\mathbf{T}_{c,d}^{(k)*} \times \sum_{w=-(N_k-1)}^{(N_k-1)} e^{-\pi|w|\Omega_k T_{\text{samp}}}(N_k-|w|)\tilde{r}^{(k)}[w]e^{j\frac{2\pi}{N_k}(q-p)w}. \quad (73)$$

Substituting (73) in (72) yields (26).

D. Proof for Result 4

We first state the following lemma about the statistics of $\mathbf{G}^{(k,k)}(p,m,p,m)$. We then we use it to simplify the expressions for $C_S^{(k)}\big(p,\mathbf{Q}^{(k)},\mathbf{Q}^{(\backslash k)}\big)$ to a special form given by Lemma 2. Lemma 3 uses this special form to lay the groundwork for applying a nulling technique first used in [10].

Lemma *1:* $\mathbf{G}^{(k,k)}(p,m,p,m)$ has the same distribution as $\mathbf{U}_R^{(k)}{\boldsymbol{\Delta}_R^{(k)}}^{1/2}\mathbf{W}{\boldsymbol{\Delta}_T^{(k)}}^{1/2}\mathbf{U}_T^{(k)\dagger}$, where $\mathbf{W}$ has i.i.d. entries with $\mathbf{W}_{i,j}\sim\mathcal{CN}(\alpha_k)$, $\forall i,j$, and

$$\alpha_k \triangleq \frac{\beta_k}{N_k Z_k M_t}\sum_{w=-(N_k-1)}^{N_k-1} e^{-\pi|w|\Omega_k T_{\text{samp}}}(N_k-|w|)\tilde{r}^{(k)}[w]. \quad (74)$$

Proof: From (73), the correlation between the $(i,c)^{\text{th}}$ and $(j,d)^{\text{th}}$ elements of $\mathbf{G}^{(k,k)}(p,m,p,m)$ is given by

$$\mathbb{E}\left[\mathbf{G}_{i,c}^{(k,k)}(p,m,p,m)\mathbf{G}_{j,d}^{(k,k)*}(p,m,p,m)\right] = \alpha_k\mathbf{R}_{i,j}^{(k)}\mathbf{T}_{c,d}^{(k)*}, \quad (75)$$

where α_k is given in (74). Hence, $\mathbf{G}^{(k,k)}(p,m,p,m)$ can be decomposed as:

$$\mathbf{G}^{(k,k)}(p,m,p,m) = {\mathbf{R}^{(k)}}^{1/2}\boldsymbol{\Psi}{\mathbf{T}^{(k)}}^{1/2}, \quad (76)$$

where $\boldsymbol{\Psi}$ has i.i.d. entries with $\boldsymbol{\Psi}_{i,j}\sim\mathcal{CN}(\alpha_k)$, $\forall i,j$. Substituting the eigen-decompositions for $\mathbf{T}^{(k)}$ and $\mathbf{R}^{(k)}$ in (76), we get

$$\mathbf{G}^{(k,k)}(p,m,p,m) = \mathbf{U}_R^{(k)}{\boldsymbol{\Delta}_R^{(k)}}^{1/2}\mathbf{U}_R^{(k)\dagger}\boldsymbol{\Psi}\mathbf{U}_T^{(k)}{\boldsymbol{\Delta}_T^{(k)}}^{1/2}\mathbf{U}_T^{(k)\dagger}. \quad (77)$$

Since the complex Gaussian distribution is rotationally invariant, $\mathbf{U}_R^{(k)\dagger}\boldsymbol{\Psi}\mathbf{U}_T^{(k)}\sim\mathbf{W}$, where $\mathbf{W}$ has i.i.d. entries with $\mathbf{W}_{i,j}\sim\mathcal{CN}(\alpha_k)$, $\forall i,j$. ∎

Let $\mathbf{Q}^{(k)} = \mathbf{U}_T^{(k)}\boldsymbol{\Omega}_k\mathbf{U}_T^{(k)\dagger}$. Thus, $\boldsymbol{\Omega}_k = \mathbf{U}_T^{(k)\dagger}\mathbf{Q}^{(k)}\mathbf{U}_T^{(k)}$. Since $\mathbf{Q}^{(k)}$ is positive semi-definite, $\boldsymbol{\Omega}_k$. Furthermore, $\text{Tr}\{\boldsymbol{\Omega}_k\} = \text{Tr}\{\mathbf{Q}^{(k)}\}$. Thus, the same constraints (34) and (35) apply to $\boldsymbol{\Omega}_k$. Substituting (30) in (33), the objective function in (30) in terms of $\boldsymbol{\Omega}_k$ is

$$C_S^{(k)}\Big(p,\mathbf{U}_T^{(k)}\boldsymbol{\Omega}_k\mathbf{U}_T^{(k)\dagger},\mathbf{Q}^{(\backslash k)}\Big) - C_I^{(k)}\Big(p,\mathbf{U}_T^{(k)}\boldsymbol{\Omega}_k\mathbf{U}_T^{(k)\dagger},\mathbf{Q}^{(\backslash k)}\Big). \quad (78)$$

Lemma *2:* The first term in (78) simplifies to

$$C_S^{(k)}\Big(p,\mathbf{U}_T^{(k)}\boldsymbol{\Omega}_k\mathbf{U}_T^{(k)\dagger},\mathbf{Q}^{(\backslash k)}\Big) = \mathbb{E}\Bigg[\log_2\Big(\det\Big[\sigma^2\mathbf{I}_{M_r} + \gamma_{\text{ICI}}^{(k)}(p)\left\langle\boldsymbol{\Omega}_k,\boldsymbol{\Delta}_T^{(k)}\right\rangle\boldsymbol{\Delta}_R^{(k)} + \sum_{l=1,l\neq k}^{K}\gamma_{\text{INI}}^{(k,l)}(p)\left\langle\mathbf{Q}^{(l)},\mathbf{T}^{(k)}\right\rangle\boldsymbol{\Delta}_R^{(k)} + {\boldsymbol{\Delta}_R^{(k)}}^{1/2}\mathbf{W}{\boldsymbol{\Delta}_T^{(k)}}^{1/2}\boldsymbol{\Omega}_k{\boldsymbol{\Delta}_T^{(k)}}^{1/2}\mathbf{W}^\dagger{\boldsymbol{\Delta}_R^{(k)}}^{1/2}\Big]\Big)\Bigg]. \quad (79)$$

The second term in (78) simplifies to

$$C_I^{(k)}\Big(p,\mathbf{U}_T^{(k)}\boldsymbol{\Omega}_k\mathbf{U}_T^{(k)\dagger},\mathbf{Q}^{(\backslash k)}\Big) = \log_2\Big(\det\Big[\sigma^2\mathbf{I}_{M_r} + \gamma_{\text{ICI}}^{(k)}(p)\left\langle\boldsymbol{\Omega}_k,\boldsymbol{\Delta}_T^{(k)}\right\rangle\boldsymbol{\Delta}_R^{(k)} + \sum_{l=1,l\neq k}^{K}\gamma_{\text{INI}}^{(k,l)}(p)\left\langle\mathbf{Q}^{(l)},\mathbf{T}^{(k)}\right\rangle\boldsymbol{\Delta}_R^{(k)}\Big]\Big). \quad (80)$$

Proof: In terms of $\boldsymbol{\Omega}_k$, the ICI covariance in (26) is given by $\mathbf{K}_{\text{ICI}}^{(k)}(p,\mathbf{Q}^{(k)}) = \gamma_{\text{ICI}}^{(k)}(p)\left\langle\mathbf{U}_T^{(k)}\boldsymbol{\Omega}_k\mathbf{U}_T^{(k)\dagger},\mathbf{T}^{(k)}\right\rangle\mathbf{R}^{(k)}$. Substituting this in (31), we get

$$C_S^{(k)}\Big(p,\mathbf{U}_T^{(k)}\boldsymbol{\Omega}_k\mathbf{U}_T^{(k)\dagger},\mathbf{Q}^{(l)}\Big) = \mathbb{E}\Bigg[\log_2\Big(\det\Big[\sigma^2\mathbf{I}_{M_r} + \gamma_{\text{ICI}}^{(k)}(p)\left\langle\mathbf{U}_T^{(k)}\boldsymbol{\Omega}_k\mathbf{U}_T^{(k)\dagger},\mathbf{T}^{(k)}\right\rangle\mathbf{R}^{(k)} + \sum_{l=1,l\neq k}^{K}\gamma_{\text{INI}}^{(k,l)}(p)\left\langle\mathbf{Q}^{(l)},\mathbf{T}^{(k)}\right\rangle\mathbf{R}^{(k)} + \mathbf{G}^{(k,k)}(p,m,p,m)\mathbf{U}_T^{(k)}\boldsymbol{\Omega}_k\mathbf{U}_T^{(k)\dagger}\mathbf{G}^{(k,k)\dagger}(p,m,p,m)\Big]\Big)\Bigg]. \quad (81)$$

By virtue of Lemma 1, (81) becomes

$$C_S^{(k)}\Big(p,\mathbf{U}_T^{(k)}\boldsymbol{\Omega}_k\mathbf{U}_T^{(k)\dagger},\mathbf{Q}^{(l)}\Big) = \mathbb{E}\Bigg[\log_2\Big(\det\Big[\sigma^2\mathbf{I}_{M_r} + \gamma_{\text{ICI}}^{(k)}(p)\left\langle\mathbf{U}_T^{(k)}\boldsymbol{\Omega}_k\mathbf{U}_T^{(k)\dagger},\mathbf{T}^{(k)}\right\rangle + \sum_{z=1,z\neq k}^{K}\gamma_{\text{INI}}^{(k,l)}(p)\left\langle\mathbf{Q}^{(l)},\mathbf{T}^{(k)}\right\rangle\mathbf{R}^{(k)} + \mathbf{U}_R^{(k)}{\boldsymbol{\Delta}_R^{(k)}}^{1/2}\mathbf{W}{\boldsymbol{\Delta}_T^{(k)}}^{1/2}\boldsymbol{\Omega}_k{\boldsymbol{\Delta}_T^{(k)}}^{1/2}\mathbf{W}^\dagger{\boldsymbol{\Delta}_R^{(k)}}^{1/2}\mathbf{U}_R^{(k)\dagger}\Big]\Big)\Bigg]. \quad (82)$$

We know that

$$\left\langle \mathbf{U}_T^{(k)}\mathbf{\Omega}_k\mathbf{U}_T^{(k)\dagger}, \mathbf{T}^{(k)} \right\rangle = \mathrm{Tr}\left\{ \mathbf{T}^{(k)\dagger}\mathbf{U}_T^{(k)}\mathbf{\Omega}_k\mathbf{U}_T^{(k)\dagger} \right\}, = \left\langle \mathbf{\Omega}_k, \mathbf{\Delta}_T^{(k)} \right\rangle. \quad (83)$$

Substituting the eigen-decomposition for $\mathbf{R}^{(k)}$ in (82), using (83), $\mathbf{I}_{M_r} = \mathbf{U}_R^{(k)}\mathbf{U}_R^{(k)\dagger}$, and the multiplicative property of the determinant yields (79). The expression for $C_I^{(k)}\Big(p, \mathbf{U}_T^{(k)}\mathbf{\Omega}_k\mathbf{U}_T^{(k)\dagger}, \mathbf{Q}^{(\backslash k)}\Big)$ follows in a similar manner. ∎

The simplified forms in (79) and (80) enable us to apply the nulling technique of [10] to optimize the precoder. Let $\mathbf{\Pi}_s$ be a diagonal matrix whose diagonal entries are 1 except for the $(s,s)^{\text{th}}$ entry, which is -1. Then, the entries of $\mathbf{\Pi}_s\mathbf{\Omega}_k\mathbf{\Pi}_s^\dagger$ are equal to those of $\mathbf{\Omega}_k$ except for the off-diagonal elements in the s^{th} row and s^{th} column, whose sign is reversed. We first get the following invariance relation.

Lemma *3:*

$$C_S^{(k)}\Big(p, \mathbf{U}_T^{(k)}\mathbf{\Pi}_s\mathbf{\Omega}_k\mathbf{\Pi}_s^\dagger\mathbf{U}_T^{(k)\dagger}, \mathbf{Q}^{(\backslash k)}\Big) = C_S^{(k)}\Big(p, \mathbf{U}_T^{(k)}\mathbf{\Omega}_k\mathbf{U}_T^{(k)\dagger}, \mathbf{Q}^{(\backslash k)}\Big). \quad (84)$$

Proof: Since the columns of $\mathbf{W}$ are statistically independent and their distribution is symmetric, $\mathbf{W}$ and $\mathbf{W}\mathbf{\Pi}_s$ have the same statistics. As a result, reversing the sign of the s^{th} column does not alter the distribution of $\mathbf{W}$. Replacing $\mathbf{\Omega}_k$ with $\mathbf{\Pi}_s\mathbf{\Omega}_k\mathbf{\Pi}_s^\dagger$ in (79), the function value remains the same. This is because the diagonal matrices ${\mathbf{\Delta}_T^{(k)}}^{1/2}$ and $\mathbf{\Pi}_s$ commute and $\left\langle \mathbf{\Omega}_k, \mathbf{\Delta}_T^{(k)} \right\rangle = \left\langle \mathbf{\Pi}_s\mathbf{\Omega}_k\mathbf{\Pi}_s^\dagger, \mathbf{\Delta}_T^{(k)} \right\rangle$. ∎

Since $C_S^{(k)}\Big(p, \mathbf{U}_T^{(k)}\mathbf{\Omega}_k\mathbf{U}_T^{(k)\dagger}, \mathbf{Q}^{(\backslash k)}\Big)$ is concave over $\mathbf{\Omega}_k$, from Jensen's inequality, we get

$$C_S^{(k)}\left(p, \mathbf{U}_T^{(k)}\left(\frac{\mathbf{\Pi}_s\mathbf{\Omega}_k\mathbf{\Pi}_s^\dagger + \mathbf{\Omega}_k}{2}\right)\mathbf{U}_T^{(k)\dagger}, \mathbf{Q}^{(\backslash k)}\right) \geq \frac{C_S^{(k)}\Big(p, \mathbf{U}_T^{(k)}\mathbf{\Pi}_s\mathbf{\Omega}_k\mathbf{\Pi}_s^\dagger\mathbf{U}_T^{(k)\dagger}, \mathbf{Q}^{(\backslash k)}\Big)}{2} + \frac{C_S^{(k)}\Big(p, \mathbf{U}_T^{(k)}\mathbf{\Omega}_k\mathbf{U}_T^{(k)\dagger}, \mathbf{Q}^{(\backslash k)}\Big)}{2}, \quad (85)$$

$$= C_S^{(k)}\Big(p, \mathbf{U}_T^{(k)}\mathbf{\Omega}_k\mathbf{U}_T^{(k)\dagger}, \mathbf{Q}^{(\backslash k)}\Big). \quad (86)$$

Furthermore,

$$\left\langle \frac{\mathbf{\Pi}_s\mathbf{\Omega}_k\mathbf{\Pi}_s^\dagger + \mathbf{\Omega}_k}{2}, \mathbf{\Delta}_T^{(k)} \right\rangle = \frac{1}{2}\left\langle \mathbf{\Pi}_s\mathbf{\Omega}_k\mathbf{\Pi}_s^\dagger, \mathbf{\Delta}_T^{(k)} \right\rangle + \frac{1}{2}\left\langle \mathbf{\Omega}_k, \mathbf{\Delta}_T^{(k)} \right\rangle, \quad (87)$$

$$= \left\langle \mathbf{\Omega}_k, \mathbf{\Delta}_T^{(k)} \right\rangle. \quad (88)$$

Thus, from (87) and (80), we can show that

$$C_I^{(k)}\left(p, \mathbf{U}_T^{(k)}\left(\frac{\mathbf{\Pi}_s\mathbf{\Omega}_k\mathbf{\Pi}_s^\dagger + \mathbf{\Omega}_k}{2}\right)\mathbf{U}_T^{(k)\dagger}, \mathbf{Q}^{(\backslash k)}\right) = C_I^{(k)}\Big(p, \mathbf{U}_T^{(k)}\mathbf{\Omega}_k\mathbf{U}_T^{(k)\dagger}, \mathbf{Q}^{(\backslash k)}\Big). \quad (89)$$

Substituting (86) and (89) in (78) yields

$$C^{(k)}\left(p, \mathbf{U}_T^{(k)}\left(\frac{\mathbf{\Pi}_s\mathbf{\Omega}_k\mathbf{\Pi}_s^\dagger + \mathbf{\Omega}_k}{2}\right)\mathbf{U}_T^{(k)\dagger}, \mathbf{Q}^{(\backslash k)}\right) \geq C^{(k)}\left(p, \mathbf{U}_T^{(k)}\mathbf{\Omega}_k\mathbf{U}_T^{(k)\dagger}, \mathbf{Q}^{(\backslash k)}\right). \quad (90)$$

The matrix $[\mathbf{\Pi}_s\mathbf{\Omega}_k\mathbf{\Pi}_s^\dagger + \mathbf{\Omega}_k]/2$ has entries equal to those of $\mathbf{\Omega}_k$ except for the off-diagonals in the s^{th} row and the s^{th} column, which are zero. Thus, nulling the off-diagonal entries of any column and the corresponding row of $\mathbf{\Omega}_k$ can only increase $C^{(k)}\left(p, \mathbf{U}_T^{(k)}\mathbf{\Omega}_k\mathbf{U}_T^{(k)\dagger}, \mathbf{Q}^{(\backslash k)}\right)$.

Repeating the same process for $s \in \{1, 2, \ldots, M_t\}$ proves that the ergodic capacity is maximized when $\mathbf{\Omega}_k$ is diagonal.

E. Derivation for Gradients in (42)

Substituting $\mathbf{Q}^{(k)} = \mathbf{U}_T^{(k)}\mathbf{P}^{(k)}\mathbf{U}_T^{(k)\dagger}$ in (80) yields

$$C_I^{(k)}\Big(p, \mathbf{U}_T^{(k)}\mathbf{P}^{(k)}\mathbf{U}_T^{(k)\dagger}, \mathbf{Q}^{(\backslash k)}\Big) = \log_2\left(\det\left[\sigma^2\mathbf{I}_{M_r} + \left(\gamma_{\text{ICI}}^{(k)}(p)\left\langle \mathbf{P}^{(k)}, \mathbf{\Delta}_T^{(k)} \right\rangle + \sum_{l=1, l\neq k}^{K}\gamma_{\text{INI}}^{(k,l)}(p)\left\langle \mathbf{U}_T^{(l)}\mathbf{P}^{(l)}\mathbf{U}_T^{(l)\dagger}, \mathbf{T}^{(k)} \right\rangle\right)\mathbf{\Delta}_R^{(k)}\right]\right). \quad (91)$$

We can show that

$$\left\langle \mathbf{U}_T^{(l)}\mathbf{P}^{(l)}\mathbf{U}_T^{(l)\dagger}, \mathbf{T}^{(k)} \right\rangle = \left\langle \mathbf{P}^{(l)}, \mathbf{\Delta}^{(k,l)} \right\rangle, \quad (92)$$

where $\mathbf{\Delta}^{(k,l)}$ is a positive semi-definite diagonal matrix whose t^{th} diagonal element is given by

$$\left[\mathbf{\Delta}^{(k,l)}\right]_{t,t} = \left[\mathbf{U}_T^{(k)\dagger}\mathbf{U}_T^{(l)}\right]_{*t}^\dagger \mathbf{\Delta}_T^{(k)}\left[\mathbf{U}_T^{(k)\dagger}\mathbf{U}_T^{(l)}\right]_{*t}. \quad (93)$$

Then, substituting (93) in (92) and taking gradients yields

$$\nabla_{\mathbf{P}^{(j)}} C_I^{(k)}\Big(p, \mathbf{U}_T^{(k)}\mathbf{P}^{(k)}\mathbf{U}_T^{(k)\dagger}, \mathbf{Q}^{(\backslash k)}\Big) = \begin{cases} \gamma_{\text{ICI}}^{(k)}(p)\xi(\mathbf{P}^{(k)}, \mathbf{P}^{(\backslash k)})\mathbf{\Delta}_T^{(k)}, & \text{if } j = k, \\ \gamma_{\text{INI}}^{(k,j)}(p)\xi(\mathbf{P}^{(k)}, \mathbf{P}^{(\backslash k)})\mathbf{\Delta}^{(k,j)}, & \text{else,} \end{cases} \quad (94)$$

where

$$\xi(\mathbf{P}^{(k)}, \mathbf{P}^{(\backslash k)}) = \sum_{t=1}^{M_r}\frac{\left[\mathbf{\Delta}_R^{(k)}\right]_{t,t}}{\left(\begin{array}{c}\sigma^2 + \gamma_{\text{ICI}}^{(k)}(p)\left\langle \mathbf{P}^{(k)}, \mathbf{\Delta}_T^{(k)} \right\rangle\left[\mathbf{\Delta}_R^{(k)}\right]_{t,t} \\ + \sum_{l=1, l\neq k}^{K}\gamma_{\text{INI}}^{(k,l)}(p)\left\langle \mathbf{P}^{(l)}, \mathbf{\Delta}^{(k,l)} \right\rangle\left[\mathbf{\Delta}_R^{(k)}\right]_{t,t}\end{array}\right)}. \quad (95)$$

REFERENCES

[1] T. V. S. Sreedhar and N. B. Mehta, "Inter-numerology interference in mixed numerology MIMO-OFDM systems in spatially correlated, time-varying fading channels," *To appear in National Conf. Commun.*, 2025.

[2] P. Guan, D. Wu, T. Tian, J. Zhou, X. Zhang, L. Gu, A. Benjebbour, M. Iwabuchi, and Y. Kishiyama, "5G field trials: OFDM-based waveforms and mixed numerologies," *IEEE J. Sel. Areas Commun.*, vol. 35, no. 6, pp. 1234–1243, Jun. 2017.

[3] "IMT vision – framework and overall objectives of the future development of IMT for 2030 and beyond," ITU-R, Tech. Rep., 2023.

[4] X. Zhang, L. Zhang, P. Xiao, D. Ma, J. Wei, and Y. Xin, "Mixed numerologies interference analysis and inter-numerology interference cancellation for windowed OFDM systems," *IEEE Trans. Veh. Technol.*, vol. 67, no. 8, pp. 7047–7061, Aug. 2018.

[5] H. Son, G. Kwon, H. Park, and J. S. Park, "Massive MIMO precoding for interference-free multi-numerology systems," *IEEE Trans. Veh. Technol.*, vol. 71, no. 9, pp. 9765–9780, Sep. 2022.

[6] L.-H. Shen, C.-Y. Su, and K.-T. Feng, "CoMP enhanced subcarrier and power allocation for multi-numerology based 5G-NR networks," *IEEE Trans. Veh. Technol.*, vol. 71, no. 5, pp. 5460–5476, May 2022.

[7] Z. Wang and V. W. S. Wong, "Joint resource block allocation and beamforming with mixed-numerology for eMBB and URLLC use cases," in *Proc. Globecom*, Dec. 2021, pp. 1–6.

[8] K. Boutiba, M. Bagaa, and A. Ksentini, "Radio resource management in multi-numerology 5G new radio featuring network slicing," in *Proc. ICC*, Aug. 2022, pp. 359–364.

[9] T. V. S. Sreedhar and N. B. Mehta, "Inter-numerology interference in mixed numerology OFDM systems in time-varying fading channels with phase noise," *IEEE Trans. Wireless Commun.*, vol. 22, no. 8, pp. 5473–5485, Aug. 2023.

[10] A. M. Tulino, A. Lozano, and S. Verdu, "Capacity-achieving input covariance for single-user multi-antenna channels," *IEEE Trans. Wireless Commun.*, vol. 5, no. 3, pp. 662–671, Mar. 2006.

[11] A. Stamoulis, S. N. Diggavi, and N. Al-Dhahir, "Intercarrier interference in MIMO OFDM," *IEEE Trans. Signal Process.*, vol. 50, no. 10, pp. 2451–2464, Oct. 2002.

[12] T. C. W. Schenk, X.-J. Tao, P. F. M. Smulders, and E. R. Fledderus, "On the influence of phase noise induced ICI in MIMO OFDM systems," *IEEE Commun. Lett.*, vol. 9, no. 8, pp. 682–684, Aug. 2005.

[13] M. Chung, L. Liu, and O. Edfors, "Phase-noise compensation for OFDM systems exploiting coherence bandwidth: Modeling, algorithms, and analysis," *IEEE Trans. Wireless Commun.*, vol. 21, no. 5, pp. 3040–3056, May 2022.

[14] X. Cheng, K. Xu, and S. Li, "Compensation of phase noise in uplink massive MIMO OFDM systems," *IEEE Trans. Wireless Commun.*, vol. 18, no. 3, pp. 1764–1778, Mar. 2019.

[15] C.-Y. Su, C.-H. Fang, L.-H. Shen, and K.-T. Feng, "Effective capacity maximization for multi-numerology based 5G NR networks," in *Proc. VTC (Fall)*, Nov. 2020, pp. 1–5.

[16] E. Memisoglu, A. B. Kihero, E. Basar, and H. Arslan, "Guard band reduction for 5G and beyond multiple numerologies," *IEEE Commun. Lett.*, vol. 24, no. 3, pp. 644–647, Mar. 2020.

[17] H. Son, K. Girim, H. Park, and J. S. Park, "Signal model and linear combining design for multi-numerology massive MIMO systems," *To appear in IEEE Trans. Veh. Technol.*, 2024.

[18] X. Cheng, R. Zayani, H. Shaiek, and D. Roviras, "Analysis and cancellation of mixed-numerologies interference for massive MIMO-OFDM UL," *IEEE Wireless Commun. Lett.*, vol. 9, no. 4, pp. 470–474, Apr. 2020.

[19] ——, "Inter-numerology interference analysis and cancellation for massive MIMO-OFDM downlink systems," *IEEE Access*, vol. 7, pp. 177 164–177 176, Dec. 2019.

[20] T. V. S. Sreedhar and N. B. Mehta, "Refined bounds for inter-carrier interference in OFDM due to time-varying channels and phase noise," *IEEE Wireless Commun. Lett.*, vol. 11, no. 12, pp. 2522–2526, Dec. 2022.

[21] C.-Y. Hsu and W.-R. Wu, "Low-complexity ICI mitigation methods for high-mobility SISO/MIMO-OFDM systems," *IEEE Trans. Veh. Technol.*, vol. 58, no. 6, pp. 2755–2768, Jul. 2009.

[22] Y. Zhang, J. Li, and L. Pang, "A scheme for cancelling intercarrier interference using partial response encoding for MIMO-OFDM systems," in *Proc. PIMRC*, Apr. 2010, pp. 241–245.

[23] K. Gopala and D. Slock, "MIMO OFDM capacity maximizing beamforming for large doppler scenarios," in *Proc. SPAWC*, Jul. 2016, pp. 1–6.

[24] ——, "Robust MIMO OFDM transmit beamformer design for large doppler scenarios under partial CSIT," in *Proc. ICASSP*, Mar. 2017, pp. 3559–3563.

[25] TR 38.901, "Study on channel model for frequencies from 0.5 to 100 GHz," 3rd Generation Partnership Project (3GPP), TR v16.1.0, 2020.

[26] H. Chen, J. Hua, F. Li, F. Chen, and D. Wang, "Interference analysis in the asynchronous f-OFDM systems," *IEEE Trans. Commun.*, vol. 67, no. 5, pp. 3580–3596, May 2019.

[27] J. Mao, L. Zhang, P. Xiao, and K. Nikitopoulos, "Interference analysis and power allocation in the presence of mixed numerologies," *IEEE Trans. Wireless Commun.*, vol. 19, no. 8, pp. 5188–5203, Aug. 2020.

[28] A. B. Kihero, M. S. J. Solaija, and H. Arslan, "Inter-numerology interference for beyond 5G," *IEEE Access*, vol. 7, pp. 146 512–146 523, Oct. 2019.

[29] L. Marijanović, S. Schwarz, and M. Rupp, "Intercarrier interference of multiple access UFMC with flexible subcarrier spacings," in *Proc. Eur. Signal Process. Conf.*, Oct. 2017, pp. 888–892.

[30] J. Mao, A. Farhang, L. Zhang, Z. Chu, P. Xiao, and S. Gu, "Interference analysis in multi-numerology OFDM systems: A continuous-time approach," in *Proc. ICC Workshop*, Jun. 2021, pp. 1–6.

[31] J. Choi, B. Kim, K. Lee, and D. Hong, "A transceiver design for spectrum sharing in mixed numerology environments," *IEEE Trans. Wireless Commun.*, vol. 18, no. 5, pp. 2707–2721, May 2019.

[32] L. Zhang, A. Ijaz, P. Xiao, A. Quddus, and R. Tafazolli, "Subband filtered multi-carrier systems for multi-service wireless communications," *IEEE Trans. Wireless Commun.*, vol. 16, no. 3, pp. 1893–1907, Mar. 2017.

[33] E. Dahlman, S. Parkvall, and J. Skold, *5G/5G-Advanced: The Next Generation Wireless Access Technology*, 3rd ed. Academic Press, Inc., 2024.

[34] C. Johnson, *5G New Radio in Bullets*, 1st ed., 2019.

[35] Z. Wang, P. Babu, and D. P. Palomar, "A low-complexity algorithm for OFDM phase noise estimation," in *Proc. SPAWC*, Jul. 2017, pp. 1–5.

[36] F. Linsalata and N. Ksairi, "On the joint estimation of phase noise and time-varying channels for OFDM under high-mobility conditions," in *Proc. ICASSP*, Jun. 2023, pp. 1–5.

[37] A. J. Goldsmith, *Wireless Communications*, 2nd ed. Cambridge Univ. Press, 2005.

[38] TS 38.521-4, "User equipment (UE) conformance specification; Radio transmission and reception; Part 4: Performance," 3rd Generation Partnership Project (3GPP), Tech. Rep. v16.6.0, 2021.

[39] R. W. Heath Jr. and A. Lozano, *Foundations of MIMO Communication*, 1st ed. Cambridge Univ. Press, 2018.

[40] D. Tse and P. Viswanath, *Fundamentals of Wireless Communication*, 1st ed. Cambridge Univ. Press, 2005.

[41] L. You, J. Xiong, X. Yi, J. Wang, W. Wang, and X. Gao, "Energy efficiency optimization for downlink massive MIMO with statistical CSIT," *IEEE Trans. Wireless Commun.*, vol. 19, no. 4, pp. 2684–2698, Apr. 2020.

[42] R. Srikant and L. Ying, *Communication Networks: An Optimization, Control, and Stochastic Networks Perspective*, 1st ed. Cambridge Univ. Press, 2013.

[43] H. H. Kha, H. D. Tuan, and H. H. Nguyen, "Fast global optimal power allocation in wireless networks by local D.C. programming," *IEEE Trans. Commun.*, vol. 11, no. 2, pp. 510–515, Feb. 2012.

[44] R. Li, S. Sun, and M. Tao, "Ergodic achievable rate maximization of RIS-assisted millimeter-wave MIMO-OFDM communication systems," *IEEE Trans. Wireless Commun.*, vol. 22, no. 3, pp. 2171–2184, Mar. 2023.

[45] L. You, J. Xiong, Y. Huang, D. W. K. Ng, C. Pan, W. Wang, and X. Gao, "Reconfigurable intelligent surfaces-assisted multiuser MIMO uplink transmission with partial CSI," *IEEE Trans. Wireless Commun.*, vol. 20, no. 9, pp. 5613–5627, Sep. 2021.

[46] L. You, J. Xiong, A. Zappone, W. Wang, and X. Gao, "Spectral efficiency and energy efficiency tradeoff in massive MIMO downlink transmission with statistical CSIT," *IEEE Trans. Signal Process.*, vol. 68, pp. 2645–2659, Apr. 2020.